Deciphering the Structure and Chemical Composition of Drug Nanocarriers: From Bulk Approaches to Individual Nanoparticle Characterization

Maeva Chaupard, Marta de Frutos, Ruxandra Gref

▶ **To cite this version:**

Maeva Chaupard, Marta de Frutos, Ruxandra Gref. Deciphering the Structure and Chemical Composition of Drug Nanocarriers: From Bulk Approaches to Individual Nanoparticle Characterization. Particle & Particle Systems Characterization, 2021, 38 (9), pp.2100022. 10.1002/ppsc.202100022 . hal-03365457

HAL Id: hal-03365457
https://hal.science/hal-03365457

Submitted on 6 Oct 2021

HAL is a multi-disciplinary open access archive for the deposit and dissemination of scientific research documents, whether they are published or not. The documents may come from teaching and research institutions in France or abroad, or from public or private research centers.

L'archive ouverte pluridisciplinaire **HAL**, est destinée au dépôt et à la diffusion de documents scientifiques de niveau recherche, publiés ou non, émanant des établissements d'enseignement et de recherche français ou étrangers, des laboratoires publics ou privés.

Title : Deciphering the structure and chemical composition of drug nanocarriers : from bulk approaches to individual nanoparticle characterization

Authors : Maeva Chaupard [1,2], Marta de Frutos [1], Ruxandra Gref [2*]*

1 Laboratoire de Physique des Solides, CNRS, UMR 8502, Université Paris-Saclay, F-91405 Orsay, France

2 Institut des Sciences Moléculaires d'Orsay, CNRS, UMR 8214, Université Paris-Saclay, F-91405 Orsay, France

Keywords: drug nanocarrier; single particle characterization; nanomedicine; spectromicroscopy; cell interaction.

Abstract: Drug nanocarriers (NCs) with sizes usually below 200 nm are gaining increasing interest in the treatment of severe diseases such as cancer and infections. Characterization methods to investigate the morphology and physicochemical properties of multifunctional NCs are key in their optimization and in the study of their *in vitro* and *in vivo* fate. Whereas a variety of methods has been developed to characterize "bulk" NCs in suspension, the scope of this review is to describe the different approaches for the NC characterization on an individual basis, for which fewer techniques are available. We put the accent on methods devoid of labelling which could lead to artefacts. For each characterization method, the principles and approaches to analyze the data are presented in an accessible manner. Aspects related to sample preparation to avoid artefacts are indicated, and emphasis is put on examples of applications. NC characterization on an individual basis allows gaining invaluable information in terms of quality control, on: i) NC localization and fate in biological samples; ii) NC morphology and crystallinity; iii) distribution of the NC components (drugs, shells), and iv) quantification of NCs' chemical composition. The individual characterization approaches are expected to gain increasing interest in the near future.

Short biographies of the authors

Dr. Ruxandra Gref is research director at CNRS, responsible of the "NanoBio" team in the Institute of Molecular Sciences, Paris-Saclay University, France. Her interdisciplinary research is focused on the design, synthesis, characterization and biological evaluation of "cage" nanomedicines with application in the treatment of cancer and resistant infections. She was among the pioneers to develop "stealth" nanoparticles to escape the recognition by the immune system, and hybrid metal-organic frameworks nanoparticles for drug delivery. Dr. Gref is interested in multifunctional "all in one" nanocarriers, where both incorporated drugs and their vehicle play synergic roles in fighting the disease.

Dr. Marta de Frutos is a researcher at CNRS, working in the Laboratoire de Physique des Solides, Paris-Saclay University, France. Her interdisciplinary research focuses on the development and use of analytical approaches based on scanning transmission electron microscopy (STEM) for the structural and chemical characterization at the sub-nanometer scale of biomaterials, nanomaterials, biological and medical systems. She has an extensive experience in Electron Energy-Loss Spectroscopy (EELS) on sensitive specimens. Her current interest includes the investigation of the physico-chemical properties of synthetic and natural hybrid organic-inorganic materials to elucidate their formation mechanisms.

Maeva Chaupard obtained a chemistry master's degree from Sorbonne University (Pierre and Marie Curie) in 2020. She is currently a Ph.D. student working under the supervision of Dr. Marta De Frutos and Dr. Ruxandra Gref at Paris-Saclay University, France. Her main interests include the synthesis and characterization of drug-loaded nanoparticles with applications in the field of nanomedicine. She is focusing her research on the in-depth characterization of biocompatible hybrid metal-organic frameworks nanoparticles. In particular, she uses advanced STEM-EELS and AFM-IR spectromicroscopies to unravel the structural and chemical properties of the nanoparticles, as well as their intracellular fate.

1. Introduction

Progress in nanomedicine has led over the last five decades to the discovery of drug nanocarriers able to efficiently incorporate, protect towards degradation and ferry the active molecules from the administration site to their target (diseased organs, tissues and cells). Drug nanocarriers improved the payload's pharmacokinetics and contributed to achieve the desired pharmacological response at the target. They are now widely exploited for therapeutic purposes, including the treatment of severe diseases such as cancer and infections.[1] A plethora of natural and synthetic materials have been engineered at a nanoscopic level and explored for drug delivery (**Figure 1**). Liposomes, the first nanotechnology-based drug delivery system, were discovered early in the 1960s.[2] The first Food and Drug Administration (FDA)-approved nanotechnology was the liposomal Doxil formulation designed for the treatment of Kaposi's sarcoma and since then, more than twenty liposomal and lipid-based formulations have been approved by regular authorities.[3] Many other types of drug nanocarriers have been developed, including polymeric, hybrid or metal nanoparticles (NPs), nanogels, dendrimers, quantum dots, carbon nanotubes (CNTs) and micelles (Figure 1). Several nanotechnologies containing an active molecule or a drug combination, such as Onpattro and Vyxeos, were FDA-approved in recent years, demonstrating the potential of nanomedicine and the growing interest in this field.[4][5] Moreover, the FDA-approved NP-based vaccines represent a giant step in the fight against the COVID-19 pandemic.[6]

Nowadays, a large variety of materials is used to prepare drug nanocarriers: ***i)*** organic compounds (lipids, synthetic or natural polymers, biomolecules); ***ii)*** inorganic materials (silica, carbon networks, metals, or metal oxides) and ***iii)*** hybrid organic-inorganic networks combining the properties of both their organic and inorganic counterparts. Generally, drug nanocarriers have a core-shell structure: ***i)*** the cores incorporate the drugs and release them in a controlled manner and ***ii)*** the shells govern the interactions with the living media (control protein adsorption, avoid recognition by the immune system, allow targeting diseased tissues and organs, confer bio-adhesion properties). Organic compounds remain the most employed materials for drug incorporation and for engineering multifunctional shells. Additionally, the presence of metals in drug nanocarriers' composition offers new functionalities, such as antibacterial or antifungal properties,[7] radioenhancement[8] or imaging abilities for personalized therapies.[9] More recently, nanoscale hybrid metal-organic frameworks (MOFs) emerged as versatile materials for drug delivery and theragnostic in reason of their intrinsic properties as contrast agents for imaging.[10]

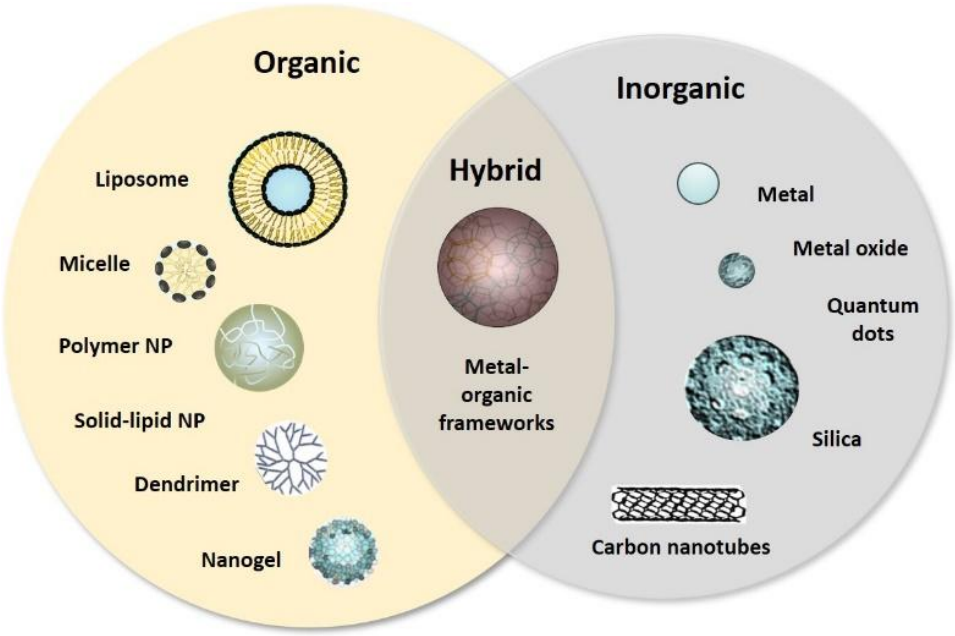

Figure 1. Schematic representation of the main drug nanocarriers classified according to their composition: organic, inorganic or hybrid organic-inorganic.

The architectures of the core-shell drug nanocarriers (NCs) are complex as they combine several functionalities among: drug co-incorporation, imaging properties for theragnostic, targeting abilities, stimuli-responsiveness, on demand drug release and triggered degradation.[11] The fast growing field of nanomedicine is in need for reliable, cutting-edge methods devoid of artefacts to investigate the morphology and physicochemical properties of the complex core-shell drug nanocarriers.

It is well recognized that the physicochemical properties of NCs play a major role in their interactions with the biological milieu. Several parameters (size, shape, surface charge and chemistry, roughness, porosity, elasticity, and many others) influence the NC' biological identity, their *in vivo* interactions with biological barriers and ultimately the therapeutic index of the drug cargo. Once administered *in vivo*, a protein corona forms rapidly at the surface of the NCs.[12] The NCs can get engulfed inside cells through direct fusion with the plasma membrane or by various endocytic pathways.[13]–[15] The cell entry mechanisms and more globally, the NCs' distribution in tissues and organs are investigated in most of the cases by labelling the NCs with fluorescent molecules. However, it is well documented that the label molecules can sometimes profoundly alter the NC's physicochemical properties, or they can leak out or be transferred from the NCs to biological tissues, leading to artefacts.[16]–[18] It is therefore important to develop and use reliable methods to detect the NCs in their biological

environment without the need of labelling.

In a nutshell, characterization methods are key in the design of core-shell drug NCs and in the study of their *in vitro* and *in vivo* fate. However, despite the huge progresses in the synthesis of novel materials and in the development of preparation methods for NCs, several aspects related to NC characterization are still not tackled. For instance, the homogeneity of the NC formulations should be assessed in terms of both size and composition. Significant variations in composition (drug loading) could render only a fraction of the NCs therapeutically active.[19][20] Indeed, individual drug-loaded NCs might drastically differ in terms of composition and/or drug location.[21] These factors are not only important for quality control, but they also play a major role on the release mechanism and the interplay with biological media.

Whereas well-established methods are routinely used to determine the NC's size distribution and polydispersity, the techniques to assess the chemical composition of individual NCs are still in their infancy. However, it is important but very challenging to chemically map the locations of the incorporated drugs and of the targeting ligands. For example, drug location (in the NC' top layers or/and embedded in the cores) determines the drug release mechanism (diffusion/desorption/degradation related). Other crucial parameters govern the NC fate in biological media, such as the homogeneity of the coatings and the successful grafting of targeting ligands onto each NC's surface. Mapping the chemical composition and the structure (morphology, crystallinity) of individual NCs is a hard task given their small size (generally less than 200 nm) and complex core-shell composition, but a crucial one to ensure the successful transfer of scientific knowledge in nanomedicine to industrial real- world applications.

In terms of quality control, an in-depth characterization of *individual* NCs is key in optimizing their formulation and uses. The aim of this review is to give a comprehensive overview of the methods available to investigate NCs structures and compositions, with special emphasis on those allowing to characterize individual NCs and to detect them in biological media without labelling. Therefore, the methods to study the NC fate *in vitro* and *in vivo* using fluorescent dyes such as confocal or super-resolution microscopies are not reviewed here.

The current techniques that enable the measurement of the most fundamental NC properties such as size distribution, shape and surface properties (charge and chemical composition) are presented in the first part of **Table 1**, highlighting their advantages and main limits. These techniques are qualified as "bulk" as they give average information on a large

population of NCs. Important properties are obtained such as size distribution, polydispersity, chemical composition, surface charge, crystallinity and porosity. In the second part of Table 1 are presented the methods adapted for individual NC characterization. The review focusses on these last methods, with special emphasis on examples of applications, principles of the methods, different approaches to analyze the data for a same technique, as well as aspects related to sample preparation to avoid artefacts.

Table 1. Main "Bulk" and individual methods used for NC characterization.

Method	Principle/advantages	Information	Limits/inconveniences
		"Bulk" methods	
Dynamic Light Scattering (DLS)	Measurement *in situ* of the fluctuations of the scattered light by NC in Brownian motion	Rapid evaluation of size distribution	Highly biased towards larger particles in suspension; cannot distinguish particle types and provides no information on shape; measurements can be concentration-dependent; no chemical information; not suitable for *in vitro/in vivo* investigations
Zeta potential	Measurement *in situ* of the potential difference between the dispersion medium and the stationary layer of fluid attached to the NC	Rapid, typically combined with DLS	Requires low NC concentrations and low ionic strength
High Performance Liquid Chromatography (HPLC)	Chromatographic separation of drug(s) and their possible metabolites	Gives reliable information of NC composition (drug loading and release) and drug integrity	Trained users; needs to set up analysis methods
Spectroscopies: Fourier Transform Infrared spectroscopy (FTIR); Ultraviolet-visible Spectrophotometry (UV-vis);	Relatively user-friendly methods routinely used to characterize NCs and drug release	Give information on NC chemical composition and interactions drug-matrix; oxidation state, symmetry, surface spins, magnetic ordering and anisotropy	In some cases, need the use of large samples and/or sample dehydration

Mössbauer; Solid and liquid Nuclear Magnetic Resonance (NMR)			
Thermogravimetric Analysis (TGA)	Provides information about mass loss during heating	Composition (drug loading, amount of coating material)	Reduced sensitivity in the case of low drug loadings; not reliable for complex NC
Elemental analysis; Inductively Coupled Plasma-Mass Spectroscopy (ICP-MS)	Gives information of chemical composition of the NCs	Composition (drug loading, amount of coating material)	Difficult to interpret for complex NC
Porosimetry	A dried sample is allowed to adsorb an inert gas (typically nitrogen) at liquid nitrogen temperature.	The (Brunauer, Emmett and Teller) BET theory is generally applied to interpret the adsorption data into information on the surface area and porosity	Needs extensive sample dehydration, delicate for fragile samples
Ellipsometry	Measures the change of polarization upon reflection or transmission	In the case of NPs deposited on a surface, measures film thickness, color and refractive index	Complex sample preparation, needs adhesion of NPs onto a substrate
Analytical centrifugation	Separates population with similar sizes based on their sedimentation properties	High-sensitivity; compatible with multimodal population; distinguish between different populations	High-cost equipment; highly trained users
Field flow fractionation (FFF)	Separates populations of NCs which are eluted in a narrow	Highly tunable (different accumulation forces can be used);	Sample recovery and choice of experimental parameters can be

	channel on which a field (thermal, electric, magnetic, hydraulic, gravitational) is perpendicularly applied	provides monodisperse sample fractions	challenging; highly trained users; needs diluted NC suspensions
X-Ray Diffraction (XRD) and Small Angle X-rays Scattering (SAXS)	Give information on NC and drug crystallinities	Crystal structure, composition, crystalline grain size	Poor information if the sample is not well crystallized; need in some cases large amounts of samples; in most cases, need dried sample
X-ray Photoelectron Spectroscopy (XPS); Secondary Ion Mass Spectroscopy (SIMS), Matrix Assisted Laser Desorption Ionisation (MALDI)	Identify the elements in the NCs (elemental composition) as well as their chemical state	Give information on the composition of the top layers of the NCs	Need sample dehydration; highly trained users
"Individual" methods for NC characterization			
Scanning Tunnelling Microscopy/Spectroscopy (STM/STS)	Probes the tunnelling current with a conductive tip scanning the sample surface	Topography (size, shape), local electronic states.	Conductive surface requires: (semi-) conductive samples or conductive substrate for thin samples; only surface analysis
Atomic Force Microscopy (AFM)	Measures the tip-sample interaction forces while scanning the surface	Topography (size, shape), mapping of the nanomechanical properties. With a specific functionalization or coating, the tip can probe other interactions (electrostatic, magnetic, thermal). Imaging can be used in combination	The contact mode can induce sample damaging through shear forces. The tapping mode is used as an alternative; only surface analysis except when combined with certain spectroscopic methods

		with spectroscopic methods; useful to investigate biological samples	
Scattering type Scanning Near-field Optical Microscopy (s-SNOM)	The tip scans the sample surface and detects its optical-near-field response upon light illumination	Topography and optical properties of the sample: scattering (Tip-enhanced Raman Spectroscopy) and absorption (Nano-FTIR Spectroscopy)	Requires sample drying to prevent from water absorption, not well appropriated for poorly scattering samples, reproducibility depending on the scanning mode and the tip nature and geometry.
Photothermal-induced Resonances (PTIR or AFM-IR)	The AFM cantilever measures the fast-thermal expansion of the sample induced by pulse laser light absorption	Topography and IR absorption of the sample; adapted for *in vitro/ex vivo* investigations	Needs sample drying to prevent from water absorption; requires highly trained users
Scanning Electron Microscopy (SEM) and 3D-Scanning Electron Microscopy (3D-SEM)	Classically, images formed by detection of the back-scattered or secondary electrons generated by scanning specimen surface with a focused electron beam	Analysis of the morphology of the specimen surface. 3D analysis of large volumes with a dedicated equipment (ultramicrotome or FIB slicing). Elemental composition when combined with EDX	Limited spatial resolution and only surface analysis on classical SEM
TEM, STEM, High-resolution (HR)	Images formed by the detection of the electrons transmitted through the specimen	Size, size distribution, morphology and structure (down to atomic scale for HR), detection and localization of NPs in cells, study of the formation mechanisms. Imaging can be combined to spectroscopic measurements	High-cost equipment; highly trained users; requires thin and dried samples which might induce other artefacts during preparation protocols; beam damage on sensitive specimens

Cryo-transmission electron microscopy (Cryo-TEM)	Same principle than TEM but observation of vitrified specimens at low doses	Analysis of sensitive particles in their native (hydrated) environment. Study of growth mechanisms, dispersion and aggregation	No information on chemical composition; preparation protocols might induce artefacts
Electron Energy Loss Spectroscopy (EELS) and Energy Dispersive X-ray spectroscopy (EDX)	Spectral analysis of the signals resulting from the interaction of the electronic beam in TEM or STEM with the specimen (X-rays for EDX and inelastically scattered electrons for EELS)	Identification of the atoms composing the specimen (qualitatively and quantitatively) and their chemical state (EELS only)	Requires relatively high electron doses that makes them not compatible with very sensitive specimens
Electron tomography (ET) and single particle analysis (SPA)	Acquisition of series of tilted 2D images in TEM or STEM for ET or of collections of individual images from particles with random orientations for SPA	3D visualisation of inorganic, hybrid and organic particles. Compatible with cryo-conditions and HR	Same limitations as 2D approaches in terms of specimen preparation and damage magnified by the higher electron doses required to record an image series
Nanoparticle tracking analysis (NTA)	Analyses the Brownian motion of NPs by tracking the scattered light	Concentration and size distribution. NTA is suitable for highly polydisperse samples and can detect fluorescent particles	Requires sample dilution and highly scattering objects; detects only NPs larger than 30 nm and which do not sediment; provides no chemical nor structural information
Single Particle Extinction and	Measures the polarizability	Refractive index, size and size	High-cost equipment; highly trained

Scattering (SPES)	and optical thickness of nanoparticles passing through a flow cell	distribution. SPES can detect single NPs suspended in a complex media.	users
Tunable Resistive Pulse Sensing (TRPS)	A set of voltage and pressure drives NPs suspended in an electrolyte through a nanopore in an elastomeric membrane	Individual particle size and charge, particle concentration	Requires sample dilution and highly conductive solutions; not appropriate for highly polydispersed samples; measures particles of > 40 nm; possible nanopore blockage; requires careful calibration
Nano-Secondary Ion Mass Spectrometry (nanoSIMS)	Analyses the secondary ions generated by the sputtering of the sample surface by a focused primary ion beam	Analysis of elemental compositions. Detection of trace elements down to parts-per-billion	Usually information on the top layers; adapted mostly for metal NPs, need isotopic labelling for organic materials
X-ray spectromicroscopy	Chemical images obtained by collecting i) the transmitted X-rays and/or ii) the emitted characteristic fluorescent X-ray or electrons	Morphology and chemical composition of NCs. Mostly employed to determine the distribution and chemical changes of NCs inside cells	Highly trained users, limited number of synchrotron sources, requires thin samples (few microns) to image in the soft X-rays regime, beam damage of radiation sensitive materials, weak spatial resolution from tens to hundreds of nanometers

2. Electron microscopy approaches

Microscopies are the pillars for the characterization of drug NCs and the investigation of their interaction with biological systems. Among them, electron microscopy (EM) is the most employed method. A large panel of imaging and analytical modes is accessible based on the detection of the different signals generated by the interaction of the primary electron beam with the analyzed specimen. Images can be collected simultaneously to spectroscopic data in a multimodal manner providing both structural and chemical analysis. Analytical EM is a method of choice for the investigation of drug NCs, whatever their composition, giving access to valuable information on their morphology, structure and chemical composition. However, certain EM approaches are more suitable for the analysis of organic nanomaterials while others better meet the needs of inorganic ones. It is also important to keep in mind that EM images provide information on a small fraction of the sample that may be not representative of the whole system. A single EM image is not representative of the specimen and care should be taken to acquire a collection of images large enough to get a good description of the whole specimen.

The aim of this review is not to give an exhaustive overview of the numerous publications concerning NC studies based on EM but rather to illustrate the possibilities offered by these approaches in the investigations of these systems. Extensive EM data can be found in reviews concerning the characterization of inorganic or organic NCs[22]–[25] and their interaction with cells.[26][27] However, to the best of our knowledge, no publication resumes all EM approaches for NCs, including 2D and 3D imaging, cryo-EM and analytical modes.

2.1. Electron microscopy approaches for individual NC analysis

2.1.1. 2D imaging by SEM, TEM and STEM

Schematic representations of a scanning electron microscope (SEM), a transmission electron microscope (TEM) and a scanning transmission electron microscope (STEM) are given in (**Figure 2**). In SEM (**Figure 2A**), a focused electron beam is used to scan the specimen and the image is obtained point by point. These microscopes are usually operated at rather low voltages (typically from 500 V to 30 kV) and most commonly, the secondary electrons generated by the primary beam close to the specimen surface are collected to obtain

an image related to the surface topography. Other signals related to the chemical composition can also be measured including back-scattered electrons (sensitive to the atomic number variations), the emission of visible photons (cathodoluminescence), of X-rays (energy dispersive X-ray spectroscopy), the specimen conduction... SEM advantages are mainly the simplicity of the specimen preparation and the quick characterization of the size distribution and shape of a large variety of NPs. As an example, the facetted structures of oligonucleotide-functionalized UiO (standing for Universitetet i Oslo)-66 MOF NPs was revealed (**Figure 3A**).[28] The mean diameter of mesoporous silica NPs (MSNs) was found equal to 200–300 nm in agreement with the hydrodynamic diameter of 293 nm estimated by DLS[29] and uniform and interconnected pore channels (of 15 nm in average diameter) were observed at their surfaces (**Figure 3B**). In Eid and Azzazy, "flower-like" silver nanostructures were observed by SEM (**Figure 3C**).[30] Some other examples can be found in Klang *et al*. and Ž. Knežević *et al.*[23][31]

In SEM, the internal structure of the specimen is not accessible because the detected signal comes from the interaction of the probe with a small volume close to the surface. In contrast, in transmission microscopes, the beam goes through the sample providing information on its inner structure. This constitutes an essential advantage because it is well known that the internal structure of NCs (for instance a hollow shell or a core-shell structure) may have a strong influence on their properties and their potential applications. Another SEM limitation comes from its relatively low spatial resolution. In most studies, SEM has been used for micro-sized particles larger than the ones under the scope of the present review. Although SEM spatial resolution can approach one nanometer for the most efficient microscopes equipped with a field emission gun (FEG) as the electron source, the atomic structure is never accessible by this approach. Higher resolution analysis is provided by transmission microscopes, both in their conventional (CTEM) and scanning (STEM) modes (**Figure 2B and C** respectively). These microscopes are among the most effective tools for the structural and chemical characterization of nanomaterials from the micro-scale down to the atomic level. Accelerating voltages of 80–300 kV are typically used to ensure the transmission of the electrons through the specimen and the high resolution imaging (resolution increases with electron energy).

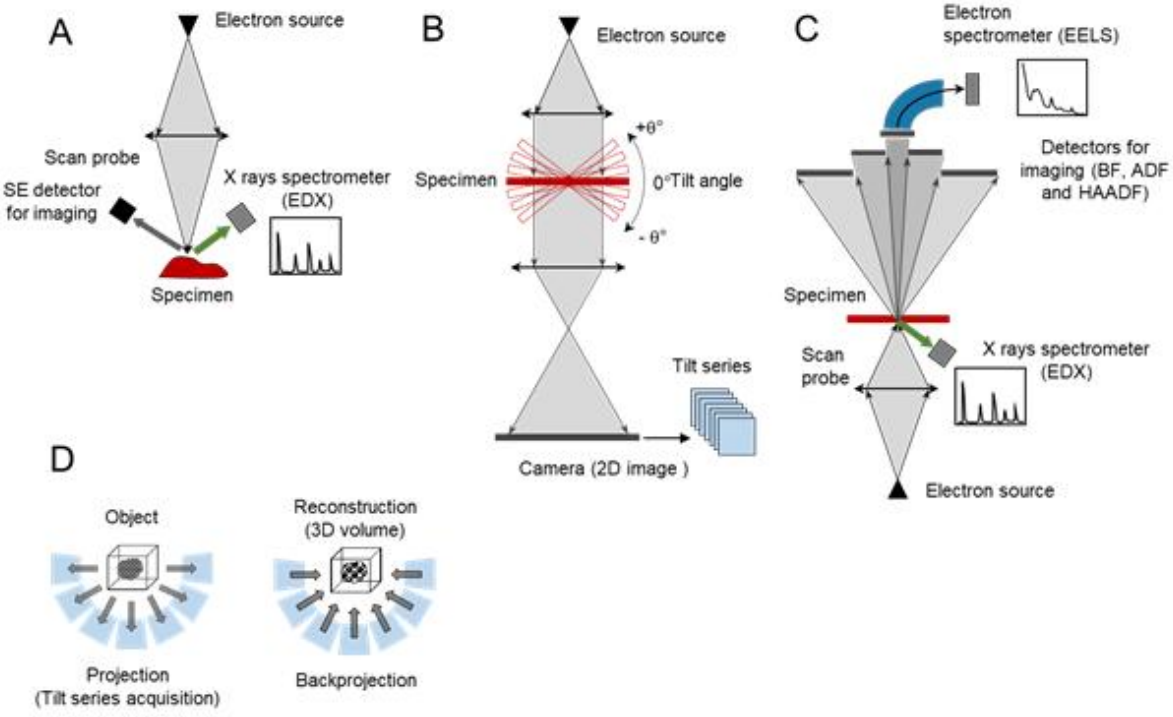

Figure 2. Schematic representations of the different electron microscopes: (A) a SEM setup including an EDX spectrometer; (B) a conventional TEM setup with the possibility to tilt the specimen for electron tomography measurements; (C) a STEM setup equipped with EELS and EDX; (D) the acquisition of a tilt series and the tomographic reconstruction.

In CTEM (or simply TEM), the complete area of interest is illuminated with a nearly parallel beam and the transmitted electrons are collected simultaneously on a CCD camera to form the image of the specimen (**Figure 2B**). The image contrast results from the local parameters such as the thickness, the atomic arrangement and the elemental composition that determine the interaction with electrons, resulting in a modification of the amplitude and/or the phase of the electron wave. An example of phase contrast imaging concerns organic NCs made of light atoms (C, N, O) that have an inherent low contrast. Based on phase-contrast imaging, high-resolution TEM (HRTEM) allows the observation of the atomic arrays in the crystalline structures of thin specimens (~100 nm). TEM provides access to the NC size, morphology and structure (**Figure 3D, E and F**) giving relevant information to analyze the influence of the different parameters during their synthesis. For instance, He and coworkers reported a drastic change of the size, morphology and mesostructure of MSNs when changing the nature of the surfactant used for their synthesis.[32] In another study, the analysis of the spherical shape and porous structure of MSNs shows that they remained unchanged after the covalent grafting of a poly(acrylic acid) (PAA) shell and platinum coating (**Figure 3D**).[33]

Silver NPs were analyzed by HRTEM revealing several morphologies associated with specific crystallographic structures (**Figure 3F**) that may have an influence on their properties.[34]

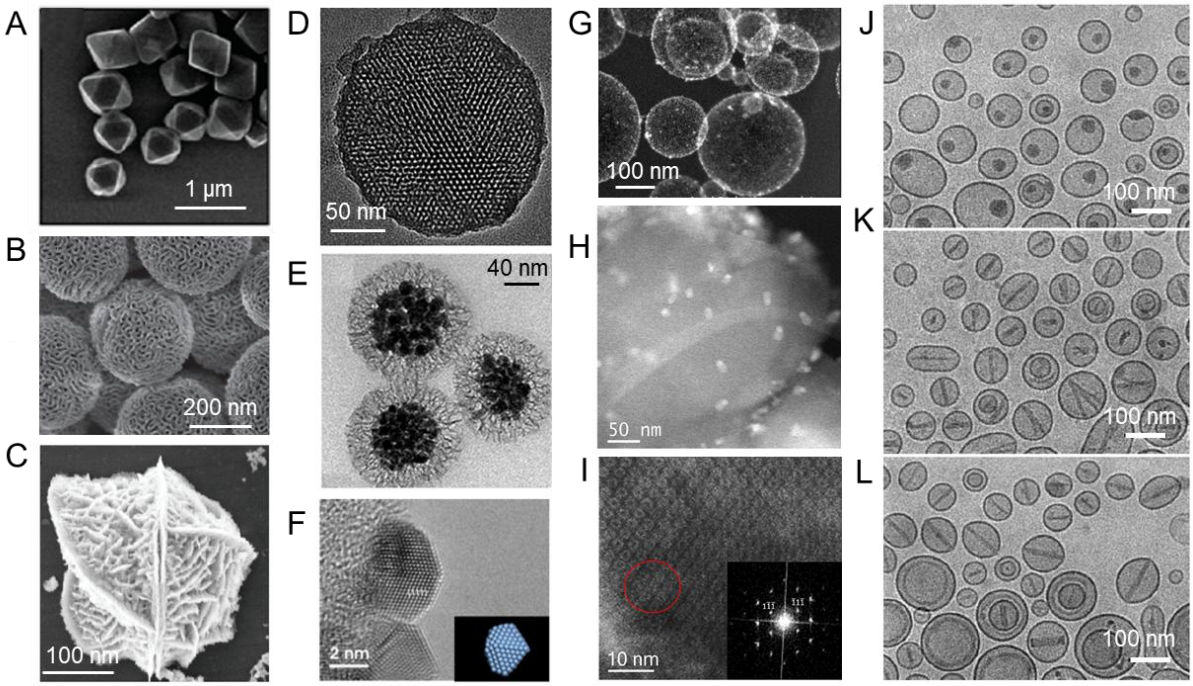

Figure 3. Examples of SEM, TEM, STEM imaging: SEM on (A) Oligonucleotide-Functionalized UiO-66 MOF NPs,[28] (B) Large-pore MSNs observed [29] and (C) hollow flower-like silver nanostructures.[30] (D) HRTEM of MSNs co-loaded with cisplatin and doxorubicin;[33] (E) TEM on mesoporous silica coated iron oxide photothermal nanoprobe;[35] (F) HRTEM on a silver NP and its respective crystallographic model given as insert;[34] (G) Cryo HAADF-STEM on metal-shell nanocapsules;[36] (H) ADF-STEM showing silver NPs associated to MIL-100(Fe) MOFs and (I) HR ADF-STEM on the MOF structure allowing the visualization of the porous system along with contrast variations related to the presence of Ag within the pores (indicated by red circle). The lattice periodicity is clearly visible as spots in the Fourier transform of the HR image (inset in I).[37] (J-L) Cryo-TEM of liposomes loaded with an iodinated amino-benzyl derivative of daunorubicin (J), the non-iodinated compound (K) and with doxorubicin (L).[38] (A) Adapted with permission.[28] Copyright 2017, American Chemical Society. (B) Adapted with permission.[29] Copyright 2014, Wiley-VCH. (C) Adapted with permission.[30] Copyright 2012, International Journal of Nanomedicine with permission from Dove Medical Press Limited. (D) Adapted with permission.[33] Copyright 2016, Royal Society of Chemistry. (E) Adapted with permission.[35] Copyright 2017, Royal Society of Chemistry. (F) Adapted with permission.[34] Copyright 2005, Institute of Physics. (G) Adapted with permission.[36] Copyright 2020, Elsevier. (H-I) Adapted under the terms and conditions of the Creative Commons Attribution License.[37] Copyright 2019, Frontiers. (J-L) Reproduced with permission.[38] Copyright 2009, Springer Nature.

In STEM (**Figure 2C**), the incident electrons also cross the sample but the beam is focused and scanned in a raster as in SEM. The STEM spatial resolution is determined by the beam size and can reach values better than 1 Å in last generation microscopes.[39] Different images are formed by collecting the electrons scattered by the specimen at different angles: the bright-field (BF) detector is an on-axis solid disc collecting the direct beam whereas Dark-field (DF) detectors are ring shaped (annular) with given inner and outer collection angles. The high-angle annular dark-field (HAADF) detector collects electrons scattered at high angle by the nucleus producing an image highly sensitive to the atomic number variations (Z-contrast images). A clear illustration of the sensitivity of HAADF-STEM imaging for heavy elements compared with TEM can be found for instance in Félix *et al.*, Morones *et al*. and Niu *et al*.[29][34][40] Light elements such as C or O are only weakly visible in the HAADF image, but are clearly seen in annular dark-field (ADF) images acquired with an annular detector with smaller collection angles. ADF is a good compromise to detect both light and heavy elements as shown in (**Figure 3H and I**) where silver NPs (bright signals) were detected inside the cages of porous iron-based MIL-100(Fe) (MIL standing for Material of Institute Lavoisier) MOFs.[37]

EM approaches impose several major constraints related to the specimen characteristics. Typically, NC suspensions are drop-casted and dried onto a TEM grid (a thin carbon film deposited on a copper grid). A first limitation comes from the high vacuum needed in an electron microscope, requiring a completely dried specimen. Another limitation comes from the specimen thickness which should be below ~500 nm to allow the beam transmission through the specimen, so observations of larger particles require sectioning by focused ion beam (FIB) or ultramicrotomy. Alternatively, the morphology of large NCs can be directly imaged in SEM if they are electrically conductive, otherwise they have to be metallized prior observations by depositing a gold or a carbon film but metallization can hide surface fine features.

EM observations at room temperature are well adapted for inorganic particles and for hybrid ones resistant to beam damage and solvent removal (as metallic, silica,…) but not for very sensitive particles as the organic ones. In all cases, drying makes impossible the analysis of the NC in their suspension medium. Environmental SEM and TEM or the use of liquid cells can help bypassing theses inconveniences, but working under partial pressure or with a

liquid imposes strong limitations in terms of equipment, resolution and accessible information.[23]

2.1.2. Cryo- approaches

Introduced in the 1980's, cryo-EM methods are a good alternative to image sensitive objects in conditions close to their native state[41][42] and constitutes a clear breakthrough for the 2D and 3D high resolution imaging of organic systems. The cryo-EM principle can be found in numerous reviews (see for instance [43]–[46]). Advantageously, the method requires only a droplet of the NP suspension which is deposited on a TEM grid and the excess of liquid is quickly removed. Then, the specimen is rapidly frozen leading to an amorphous (vitreous) thin film devoid of crystalline ice and containing the NPs. This method can be applied to all EM microscopes (**Figures 3G-L)** but they need dedicated equipment in order to avoid specimen devitrification: a cryo-holder and a sensitive detection (ideally a direct detection camera) to achieve imaging at very low electron doses.

Numerous examples illustrate the usefulness of cryo-TEM. For instance, the stability of phospholipid liposomes that is limited by hydrolysis has been studied as a function of storage time, temperature and pH.[47] The - complex lipid formulations could be optimized based on an accurate determination of their composition and phase behavior.[48] In addition, it could be revealed that the incorporated anticancer drugs (doxorubicin and a daunorubicin derivative) precipitated inside the liposomes (**Figures 3J-L**).[38] Other examples of cryo-TEM studies are reviewed by Kuntsche *et al*.[24]

The main drawback here is related to the film thickness that imposes a limit to the NP sizes which can be observed. Indeed, particles larger than the film thickness are not incorporated or may be found near the grid bars where observations are not possible. Moreover, images are usually acquired in the holes of the carbon film and since the vitreous film is thinner in the hole center, smaller particles are found in these regions as compared with the edges. Cryogenic methods are also time-consuming and costly but they are essential for the characterization of sensitive specimens as organic and certain hybrid NPs, and to study particle aggregation and dispersion.[49]

2.1.3. 3D imaging by single particle analysis and tomography

EM imaging provides two-dimensional (2D) images that are the projection of three-dimensional (3D) objects. Electron tomography (ET) and single particle analysis (SPA) are powerful techniques developed to achieve realistic 3D particle visualizations. 3D imaging by ET relies on the acquisition of a set of 2D images from the specimen by varying its orientation (tilting angles typically from -60° to +60°) relative to the incident electron beam (**Figure 2B**). The actual 3D images are obtained using mathematical algorithms to combine the information of the different projections from the tilt series (**Figure 2D**).[45][50] In SPA, the 3D reconstructions are built up from individual images of identical particles with random orientations by processing the data using iterative algorithms.[51]–[53] ET and SPA could be applied to resin embedded or frozen-hydrated specimens. In cryo-conditions, due the radiation sensitivity, image series should be acquired with minimum electron doses in order to preserve high-resolution features.[51][54]

A collection of reconstructions obtained by cryo-TEM imaging from NPs can be found in [55]. Some representative NC examples are given in **Figure 4**: SPA investigation of RNA-NPs loaded with paclitaxel for targeted cancer therapy (**Figure 4A**);[56] Cryo-ET study of the 3D architecture of phytantriol cubosomes stabilized with Tween 80 (**Figure 4B**);[57] of liposomes containing doxorubicin (**Figure 4C**)[58] and of superparamagnetic iron oxide NPs (SPIONs) within liposome membranes (**Figure 4D**).[59] Similarly, the engulfment of silica NPs in liposomes was analyzed by Cryo-ET for unveiling the dynamics of the process.[60]

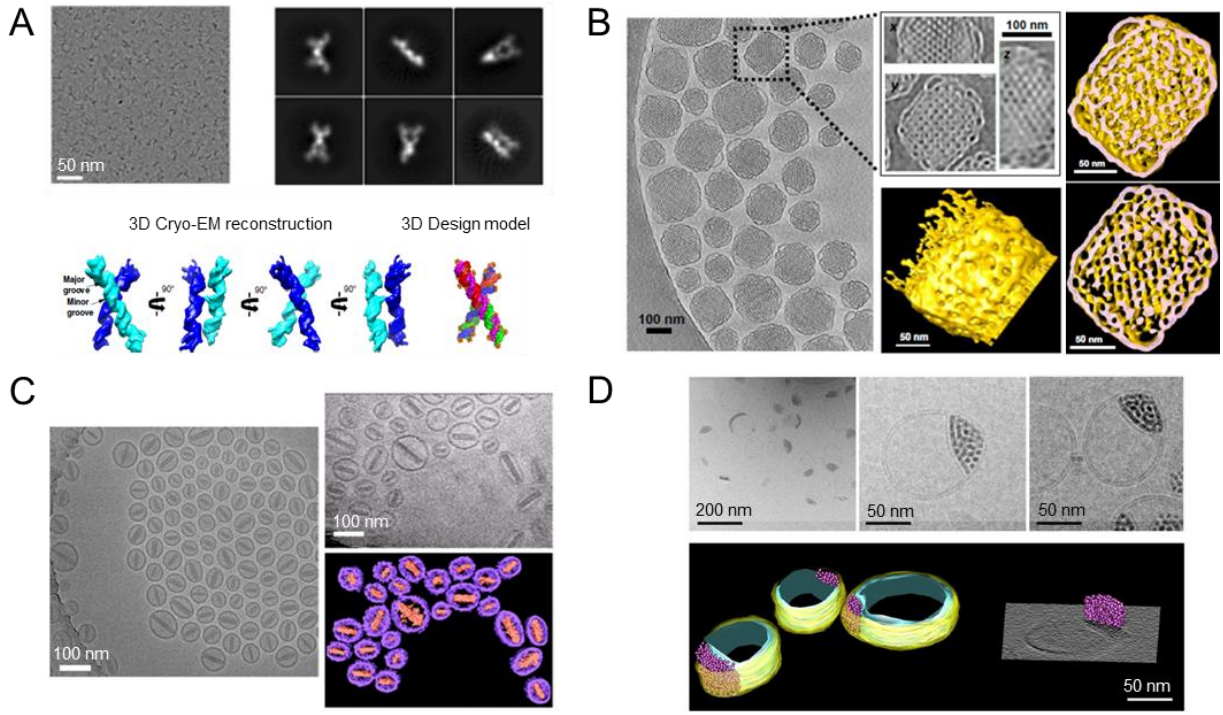

Figure 4. 3D imaging in cryo-TEM by Single Particle Analysis and Electron Tomography: (A) 3D reconstructed maps from SPA of the structure of RNA four-way junction NPs loading 24 paclitaxel molecules. A typical cryo-EM micrograph from an area showing a large number of NPs and the 2D class averages is presented.[56] 3D reconstructions from cryo-ET imaging of : (B) phytantriol cubosomes stabilized with Tween 80. Cross sections of the reconstructed particle are shown at different positions showing the water channels;[57] (C) liposomes containing doxorubicin;[58] and (D) liposomes with inclusion of SPION clusters.[59] Typical cryo-TEM images and subsequent tomographic reconstructions are shown for each system. (A) Adapted under the terms and conditions of the Creative Commons Attribution 4.0 International License.[56] Copyright 2020, Springer Nature. (B) Adapted with permission.[57] Copyright 2016, Elsevier B.V. (C) Reproduced with permission.[58] Copyright 2008, Future Medicine Ltd. (D) Reproduced with permission.[59] Copyright 2014, American Chemical Society.

In life sciences, most of the 3D studies rely on BF-TEM imaging but in material sciences, HAADF-STEM is frequently preferred for tomographic reconstructions ~~images~~ because its resolution can reach the atomic scale.[61] Moreover, TEM tomography provides reliable 3D structural information for amorphous or partially crystalline materials (with small crystalline domains), but HAADF-STEM tomography is better suited for highly crystalline materials due to its contrast proportional to the specimen thickness and density, with a negligible influence from the diffraction contrast. Due to its Z-contrast, HAADF-STEM

tomography also enables a very high sensitivity to detect small metallic particles in an organic environment.[62]

2.1.4. Analytical EM approaches (EDX, EELS, EFTEM)

EM imaging is often not sufficient to understand the morphology and the organization of heterogeneous particles made of several constituents of different chemical natures assembled together. Analytical EM approaches are ideal tools to investigate these complex systems. The most common EM analytical techniques used for chemical mapping are based on the detection of the X-rays emitted by the specimen (energy-dispersive X-ray spectroscopy, EDXS or EDX or EDS) or on the analysis of the energy lost by the incident electrons when interacting with the sample (Electron Energy Loss Spectroscopy, EELS). However, the corresponding spectroscopic signals may be orders of magnitude weaker than imaging signals. As a consequence, analytical methods require quite high electron doses that are not compatible with vitrified specimens imaged in cryo-conditions.

EDX consists of collecting the characteristic X-ray emitted when a primary electron ionizes an atom. EDX is compatible with SEM, TEM and STEM, each set up imposing the spatial resolution and sensitivity of the resulting spectroscopic data. EDX can provide qualitative, semi-quantitative or quantitative information[62] on the elements present in the specimen. Concerning NCs, this approach has been mainly applied to detect metallic compounds. For instance, the EDX signal of platinum was analyzed to check the incorporation of Cisplatin in single-walled CNTs[63] and in PAA-modified MSNs (**Figure 5A**).[33] In another study, the gold coating of iron oxide NPs (30 nm diameter) was monitored by EDX.[64]

EDX is well adapted for the elemental mapping but is not informative concerning the chemical state of the elements and more particularly on the nature of the organic components and some studies combine EDX to Fourier Transform Infrared (FTIR) spectroscopy to compensate for this lack of information. In Li *et al*.[33], MSNs were covalently grafted with a PAA shell which was further cross-linked by a platinum(II) complex which reacted with the PAA carboxyl groups giving Pt@PAA-MSN. The successful NP coating with a PAA shell was confirmed by FTIR while the reaction with the Pt(II) complex was followed by FTIR and EDX.

Alternatively, the kinetic energy of the transmitted electrons can be analyzed in a STEM by an EELS spectrometer (**Figure 2C**). As a result of the interaction with the specimen, the electrons suffering an energy loss of few tens of eV are associated to the excitation of the valence electrons ("low loss excitations") whereas higher energy losses (from 100 to 1000 eV approximately) are related to the ionization edges of the inner electrons ("core loss edges") (**Figure 5B**). Then the elements composing the specimen can be identified by their specific features but also their chemical state by analyzing the edge fine structures. Quantitative information on the relative chemical concentrations are also accessible.[65]

The probe rastering makes SEM and STEM particularly well appropriated for spectromicroscopy approaches based on the acquisition of a spectrum (EDX or EELS) at each beam position over the area of interest (the so called "spectrum-imaging mode"), giving access to the spatial distributions of the chemical compounds (chemical maps) (**Figure 5C-E**). The elemental maps of silver and gold NPs were obtained by EDX in Ristig *et al*.[66] (**Figure 5C**). The synthesis of small magnetic iron NPs (size < 10nm) was monitored by EELS to characterize the distributions of iron and gadolinium (**Figure 5D**).[67] In Mahugo *et al*.[37], silver was loaded in MIL-100(Fe) nanoscale MOFs (nanoMOFs) and a very peculiar contrast was observed for certain silver NPs together with a difference in their crystallization. EELS elemental maps reveal that this difference comes from the presence of residual chloride from MOF synthesis which associates with a fraction of silver NPs, while the rest is pure silver NPs **(Figure 5E).**

EELS maps can also be obtained in TEM by forming a filtered image with electrons of given energies (corresponding to the core-loss atomic edge). For example, the distributions of three drugs (heparin, protamine and ferumoxytol) were detected in NCs based on their respective signals of sulfur, nitrogen, and iron (**Figure 5F**).[68] In Weiss *et al*.,[69] gelatin coating was (hardly) detected on the surface of poly (lactic-co-glycolic acid) (PLGA) NPs by its weak nitrogen signal. However, energy filter TEM (EFTEM) is delicate and limited to some elements with intense edges clearly visible. Moreover, it does not allow to analyze the chemical state of the sample. Alternatively, low-loss EFTEM has been used to image organic coatings on gold NPs at ambient temperature with sufficient contrast without the need for staining.

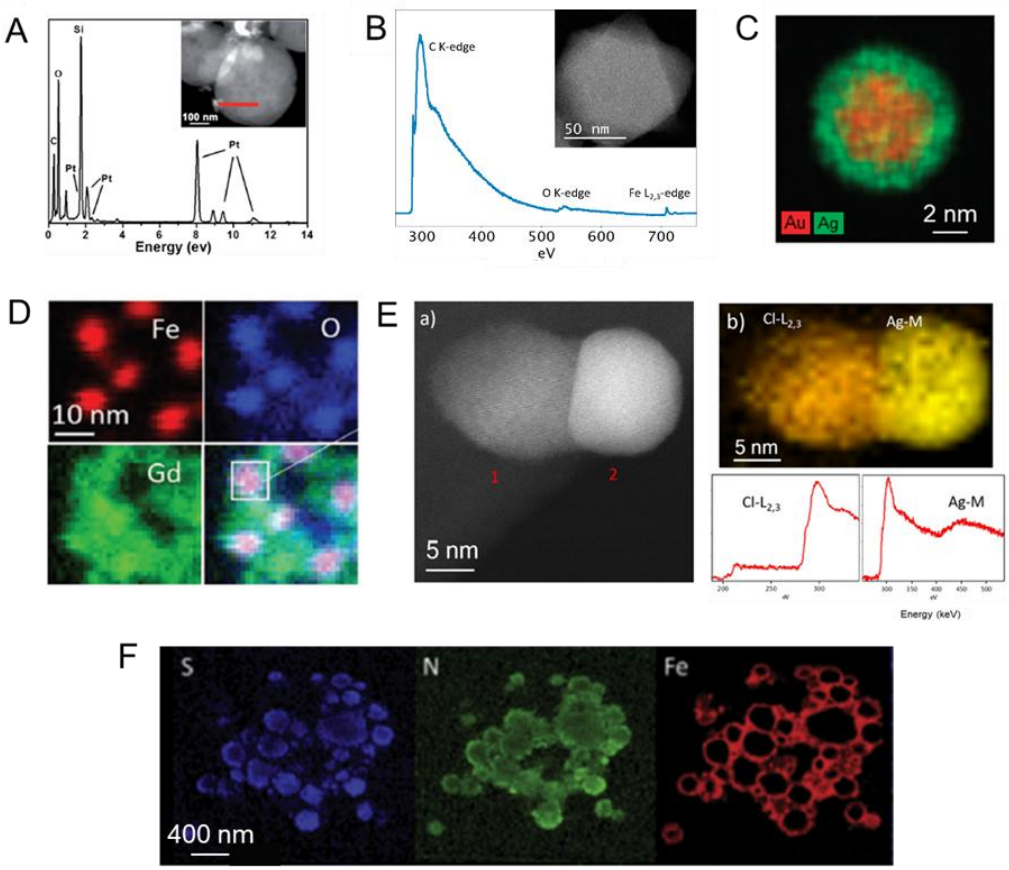

Figure 5. Data from analytical EM approaches: (A) EDX spectrum of cisplatin+doxorubicin dual-loaded MSNs with inset TEM image[33] and (B) EELS spectrum from a MIL-100(Fe) showing peaks for the ionization edges of C, O, and Fe (unpublished results). The strong peak corresponding to C can be due to the carbon film from the TEM grid and nothing can be said about the presence of carbon inside the NPs. The respective STEM image is given in inset ; (C) EDX maps from a bimetallic silver–gold NP coated with PVP for colloidal stabilization (Diameter ~6 nm);[66] (D) EELS elemental maps from FeGd-HN_3 NPs used as contrast agents for MRI. Iron (red), oxygen (blue), and gadolinium (green) maps were generated by integrating 10–20 eV windows above the respective core edges. The fourth image corresponds to the overlay of the three maps, showing all three colors.[70] (E) STEM-ADF image showing one silver particle incorporated in MIL-100(Fe) with two different regions and the associated EELS elemental maps. The different structures observed on certain silver NPs is associated with the presence of chloride (Cl in orange and Ag in yellow). The spectra are shown below for each edge;[37] (F) EFTEM maps of heparin, protamine and ferumoxytol distributions in nanocomplexes formed by mixing the three drugs. Heparin, protamine and ferumoxytol are revealed by the presence of S (blue), N (green) and Fe (red) respectively.[68] (A) Adapted with permission.[33] Copyright 2016, Royal Society of Chemistry. (C) Adapted under the terms and conditions of the Creative Commons Attribution-NonCommercial 3.0 Unported Licence.[66] Copyright 2015, Royal Society of Chemistry. (D) Adapted with permission.[70] Copyright 2018, Wiley-VCH. (E) Adapted under the terms and conditions of the Creative Commons Attribution License.[37] Copyright 2019, Frontiers. (F) Adapted with permission.[68] Copyright 2017, Elsevier.

2.1.5. Combining EM approaches for the monitoring of the NC design.

The great diversity of complementary EM approaches can be combined allowing a direct view of the NCs' sizes and shapes, crystallographic structures, chemical compositions and 3D structures. The study Wang *et al*.[28] illustrates well this complementarity. The authors investigated a strategy for functionalizing a series of different nanoMOFs based on Zr, Fe, Cr and Al with oligonucleotides. Their sizes (~ 200 nm) were first determined by SEM (**Figure 3A**). Then TEM was used to verify that the nanoMOF shapes were preserved after surface functionalization. Finally, nanoMOFs were associated with functionalized gold NPs (~ 20 nm) (**Figure 6A**). TEM and HAADF-STEM imaging coupled with EDX mapping were crucial to determine the complex morphologies of the resulting bespoken hybrid core-satellite architectures (**Figure 6B and C**).

Another interesting example is provided by Hitchcock and coworkers who aimed to prepare NCs with oily cores containing paclitaxel and metallic shells to avoid drug leakage. First, the oily droplets were stabilized with Pt NPs (Pickering emulsion) and then a gold shell was synthesized onto them. TEM and HRTEM were employed to control the size and crystallinity of the Pt NPs and to optimize the gold coating. Cryo-TEM and cryo-HAADF-STEM provided crucial information at different stages of the synthesis and in particular, the very small Pt particles (~ 5 nm) could be easily visualized at the surface of the emulsion droplets (**Figure 6D**). In addition, SEM was used to image the metal-shell microcapsules at the end of the process.[36]

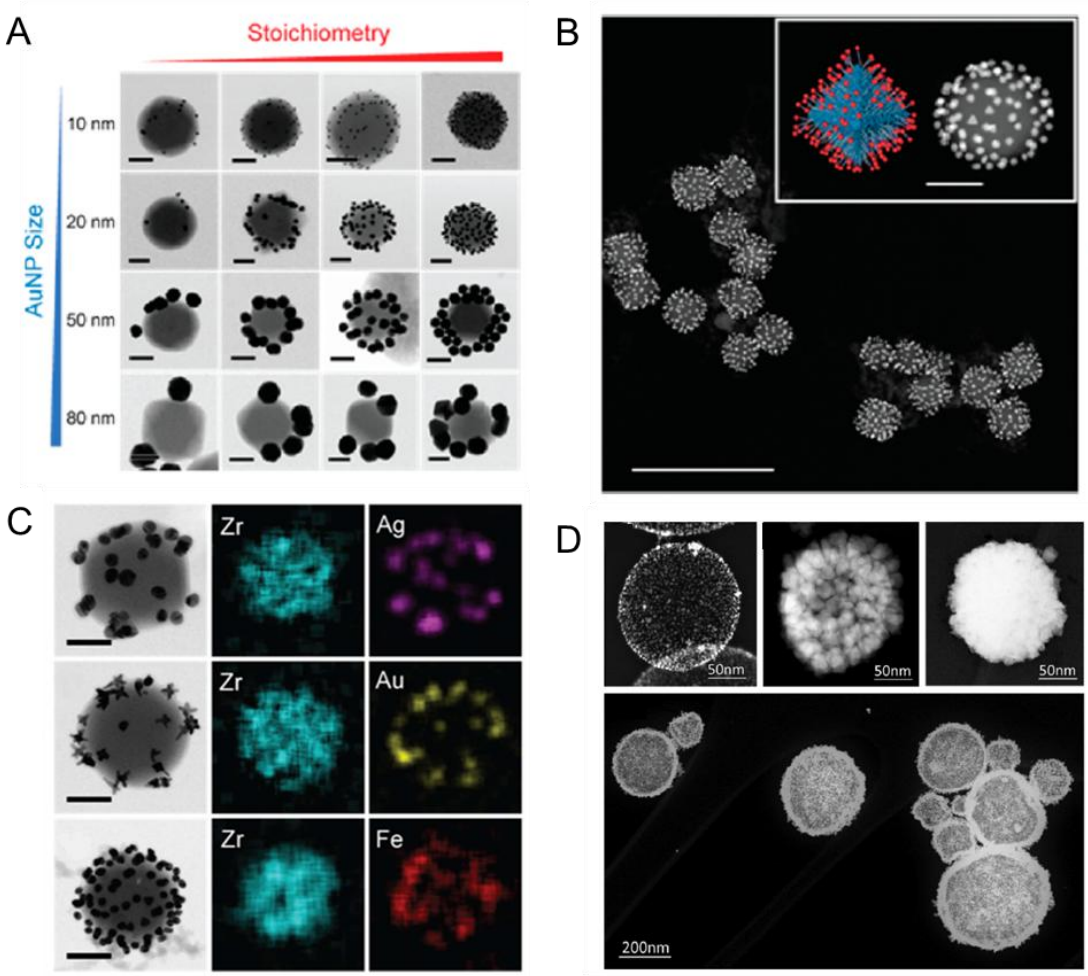

Figure 6. NC studies combining different EM approaches: (A) TEM images of nanocluster assemblies demonstrating how the DNA ligands on MOF NPs and gold NPs provide control over the structural makeup of the assemblies (scale bars = 100 nm); (B) HAADF image of nanoclusters formed from complementary 225 nm DNA-UiO-66 MOF NPs and 20 nm DNA-Au NPs. Inset: schematic illustration of a MOF - gold NP cluster and a single nanocluster (scale bar = 1µm for main figure and 100 nm for inset); (C) EDX elemental mapping showing (from top to bottom): DNA-modified silver NPs assembled around a DNA-UiO-66 MOF NP; DNA-modified gold nanostars assembled around a DNA-UiO-66 MOF NP and DNA-modified iron oxide NPs assembled around a DNA-UiO-66 MOF NP (scale bars =100 nm). Images (A-C) from Wang *et al.*[28]. (D) Cryo HAADF-STEM images on a nanoPickering emulsion drop with a gold film with increasing thickness on its surface (top images). The bottom image shows a wider field of the sample.[36] (A-C) Reproduced with permission.[28] Copyright 2017, American Chemical Society. (D) Reproduced with permission.[36] Copyright 2020, Elsevier.

2.2. Exploring NC interactions with cells by EM approaches

EM imaging is well established and widely used in biology to investigate the cellular ultrastructure (organelles and membrane structures) with an appropriate contrast and high

resolution. The combination of imaging and spectroscopic approaches constitutes an ideal tool to investigate the mechanisms of cellular uptake and the action of individual NCs on cells.

2.2.1. Cell preparation and 2D imaging by TEM and STEM

Biological environments impose constraints in terms of specimen preparation and imaging conditions. Three major limitations have to be circumvented to image NCs in cellular specimens: (i) whereas biological samples contain more than 2/3 of water, EM observations have to be done under vacuum; (ii) cells are much larger than the maximum thickness accessible by (S)TEM so they have to be sliced; (iii) the visualization of the cell features often needs contrasting agents as the intrinsic contrast of the organic biological samples is low. Many well-established preparation protocols have been developed to meet these constraints for a variety of biological specimens[46] giving reproducible and reliable data with a nanometric resolution. Standard protocols (non-cryogenic) consists of a cell fixation in order to preserve the cellular ultrastructure, a resin embedding to stiffen the soft biological sample enabling to cut the specimen into ultrathin sections (typically 50–200 nm) and a staining to highlight the low contrast features (cellular structures but also NCs in certain cases). However, when dealing with NC cellular uptake, the effect of each preparation step has to be carefully evaluated and adapted accordingly in order to preserve the NC integrity and their cellular localization.[26][27][71]

Many NCs are resistant to these protocols and are quite easily detected in the cellular context by their high contrast compared to the biological framework. The only limitation for robust particles is that the sectioning thickness has to be adjusted to their sizes. Good examples are inorganic NCs and certain hybrid NCs such as MOFs because of their chemical stability and high electron density (atomic number) compared to organic compounds. For instance, metallic magnetic NPs were easily observed in cancer cells by TEM, revealing that their localization was modulated by incubation conditions.[72] In another study, UiO nanoMOFs internalized in H460 cancer cells remained structurally intact inside endosomes **(Figure 7A)**.[73] Iron-based MIL-100(Fe) nanoMOFs co-incorporating two antibiotics were localized by TEM in *Staphylococcus aureus* infected macrophages.[74] Noticeably, some NCs colocalized with the intracellular pathogens and they degraded within a few hours **(Figure 7B)**. In Balfourier *et al*.[62], the long-term fate of gold NPs was analyzed in fibroblasts and,

against generally admitted ideas, it was shown that they were bio-dissolved forming diffuse electron-dense areas visible in TEM and STEM **(Figure 7C)**.

The main challenges arise for the intracellular observation of certain organic and hybrid NCs that may be destabilized by specimen preparation or whose identification in the cellular context is not straightforward due to their weak inherent contrast.[26][27] Depending on their functional groups, some polymeric NPs are stained efficiently by usual staining agents (uranyl acetate and lead citrate) while some others are unaffected. A strategy to enhance NC contrast consists of incorporating metal particles in the NCs but this can profoundly affect the physicochemical properties of the NCs and their interaction with cells. Other artefacts might arise from the embedding process (dehydration, chemical reactions, temperature increase for resin polymerization, pH changes). Cryogenic approaches such as high-pressure freezing constitute a good alternative by replacing the chemical fixation by a physical fixation associated with a temperature decrease.[46][75] To date, due to the experimental complexity, only a few studies dealt with NC observations in the cellular context in cryo-conditions.[76] Alternatively, a sucrose-solution was used as cryo-protectant (Tokuyasu method), enabling to study at room temperature the uptake of NCs made of poly(L-lactic acid) particles (~120 nm) decorated with 25nm-magnetite NPs in human mesenchymal stem cells and their intracellular degradation.[77] Later, it was shown that the solvents used for dehydration completely dissolved the PLGA NCs producing holes in the sections resulting in bright areas at the NC initial positions.[78]

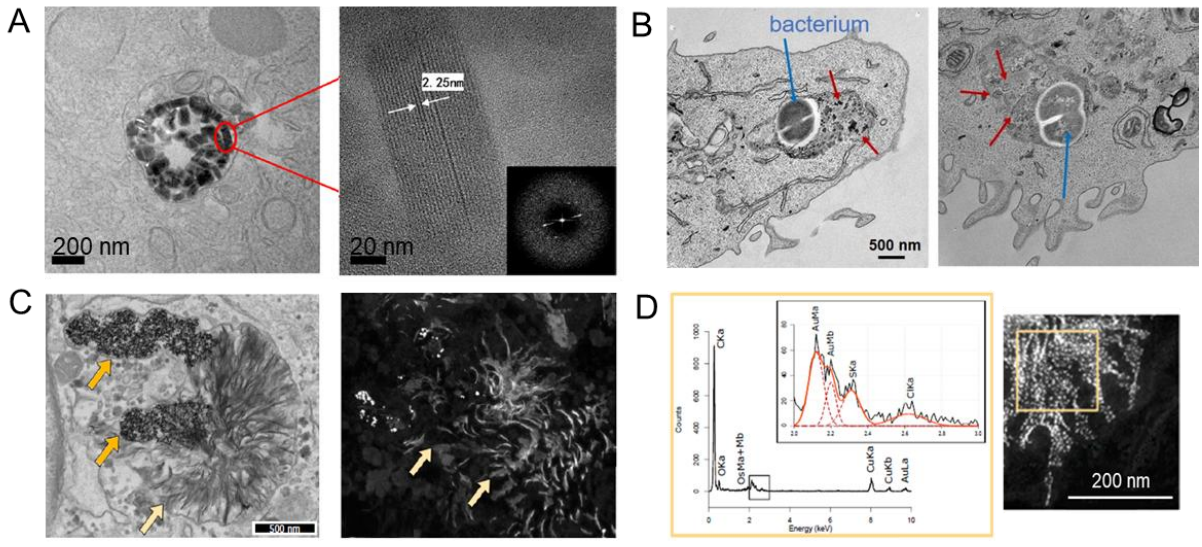

Figure 7. Analysis by EM approaches of NCs in cells: (A) TEM observations of UiO nanoMOFs in the endosomes of H460 cells. The zoomed-in view (right) of the nanoMOF marked by red circle (left) shows their structural integrity.[73] (B) TEM observations showing the internalization of drug loaded MIL-100(Fe) nanoMOFs in infected macrophages after 1h incubation (left) and after 6h (right). MOFs are indicated by red arrows and bacteria by blue ones;[74] (C) TEM (left) and STEM (right) images of human fibroblasts after 2-week exposure to 4 nm gold NPs.[62] They show the existence in lysosomes of dense and diffuse electron-dense areas resulting from the particle degradation; (D) After 2 week exposure, the analysis by EDX of the composition of the diffuse area (marked by the yellow square on the right image) reveals a specific signal of sulphur associated to gold in the degraded particles (Inset). (A) Adapted with permission.[73] Copyright 2014, American Chemical Society. (B) Adapted with permission.[74] Copyright 2019, Wiley-VCH. (C-D) Adapted with permission.[62] Copyright 2020, National Academy of Sciences.

2.2.2. Analytical EM approaches (EDX, EELS, EFTEM)

Analytical EM approaches (EDX and EELS) represent a good way to avoid ambiguities related to particle identification in the cellular context, provided that at least one element composing the NCs is not present in the cell. For instance, TEM coupled to EDX analysis was used to identify ultrafine SPIONs in MCL5 cancer cells[79] and SiO_2 NPs in human B lymphoblastoid cells (TK6) in different environments containing serum.[49] It was also helpful to localize silver NPs on gram-negative bacteria where a sulphur signal was found associated with silver.[34] Analytical EM also offers the possibility to follow the NP degradation in cells. An interesting example concerns the degradation of gold NPs in human fibroblasts.[62] After two weeks degradation, EDX analysis reveals a specific signal of sulphur associated with gold allowing the authors to propose possible degradation mechanisms (**Figure 7D**).

EELS has been more rarely used than EDX to analyze NCs in cells and very few examples are found in the literature. Allard-Vannier and coworkers investigated by EELS how folic acid-capped polyethylene glycol (PEG)ylated magnetic NPs enter in cancer cells.[80] Compared to EDX, EELS offers the advantage of a better sensitivity for light elements and the possibility to provide information concerning their chemical bonds allowing to distinguish between different compounds.[81] Despite these advantages, to the best of our knowledge, the possibility to analyze chemical bonds has not been exploited so far for the study of NCs in cells.

2.2.3. Imaging large volumes by 3D-SEM

Most EM approaches provide information on a reduced volume. This constitutes a major limitation when dealing with NCs in cells and moreover, in tissues. The probability of finding particles is very low if the incorporated quantity is small and the information may be not representative of their localization in the complete specimen. The specimen thickness has also to be adjusted to the NC sizes in order to observe them. In recent years, a revolutionary technique has emerged based on the use of SEM to determine the 3D structure of thick biological samples. As SEM by itself can only characterize the specimen surface, it was coupled with a system able to remove thin sections from the specimen surface successively and a new SEM image is recorded from the new top surface. Image stacking allowed to reconstitute the full volume of the object. Standard TEM protocols are used for specimen preparation.

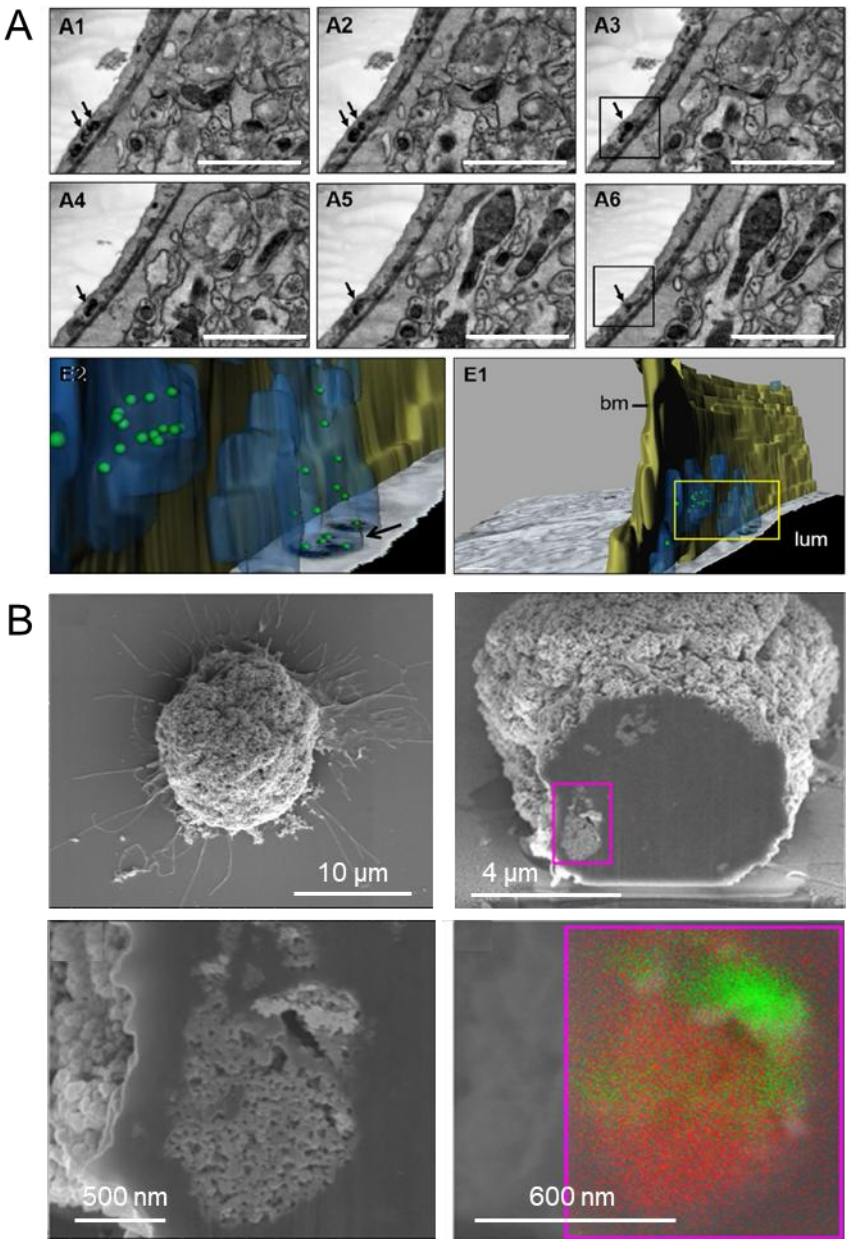

Figure 8. 3D SEM imaging: (A) the trafficking through the blood–brain barrier of gold NPs (20 nm) coated with specific antibodies (8D3) were studied by SFB-SEM. A1-A6 correspond to selected serial images from an image stack. The arrows indicate vesicles containing gold NPs. Bottom views correspond to the 3D reconstruction of the image stack. Gold NPs are represented as green spheres and the endothelial vesicles in blue (bm basal membrane, lum lumen of the capillary).[82] Scale bar = 2 µm; (B) Au@PEI-Fe_3O_4 NPs (gold NP size ~ 4 nm and Fe_3O_4 NP core size ~ 50 nm) in microglial BV2 cells. The specimen sectioning was obtained by FIB and NPs were found agglomerated on the cell membrane surface. EDX maps allow the identification of NPs in the cellular context by their signals associated with Fe (red) and Au (green).[40] (A) Adapted with permission.[82] Copyright 2017, Springer Nature. (B) Adapted under the terms and conditions of the Creative Commons Attribution 4.0 International License.[40] Copyright 2019, Springer Nature.

Two approaches have been used to slice the specimen inside the SEM chamber. In serial block-face SEM (SBF-SEM), an automated ultramicrotome is used to obtain thin sections of about 20 nm. In Cabezón *et al.*[82], SBF-SEM was applied to study the trafficking across the blood-brain barrier of gold NPs coated with specific antibodies. Au-NPs were identified inside endocytic vesicles in the brain capillary endothelial cells (**Figure 8A**). Alternatively, SEM can be combined with a FIB used as a nano-scalpel able to cut thinner sections (< 20 nm), avoiding the artefacts associated with the mechanical sectioning. The ultrastructure of spheroids and their uptake of magnetic NCs was investigated by FIB–SEM in Mollo *et al.*[83] (a video of the reconstructed volume is given in SI). In Félix *et al.*[40], small gold NPs attached to Fe_3O_4 cores were designed for hyperthermia applications and their distribution was analyzed by FIB-SEM in microglial BV2 cells. Imaging was combined to an EDX analysis in order to unambiguously identify NPs by their chemical composition (**Figure 8B**).

3. Near-field approaches

Nowadays, an increasing interest is growing towards near-field approaches. The two main near-field techniques are Scanning Tunnelling Microscopy (STM) and Atomic Force Microscopy (AFM). These rather non-destructive microscopies, based on the detection of a signal emitted nearby the sample surface, are widely employed to determine the specimen size and surface properties (conductivity, rugosity, viscoelasticity…). They consist in scanning over the sample surface a nanosized probe composed of a cantilever ended by a sharp tip. The tip acts as a near-field detector, measuring the local interactions with the sample surface. The cantilever motion generates 3D images related to the sample topography or physicochemical properties. Its x,y,z movements are enabled by applying voltage on a piezoelectric scanner which supports the cantilever. The surface scanning range can reach few hundreds of micrometers enabling the observation with a nanoscale resolution of large areas as whole cells. Both the piezoelectric crystal high sensitivity (angstrom scale) and the probe nanosize (~ 20 nm) contribute to reach a high spatial lateral resolution, down to the sub-nanometer scale under certain conditions. The vertical resolution depends only on the z-piezo scanner and can reach values as low as 0.01 nm for scanning tunnelling microscopes.

3.1. Scanning Tunnelling Microscopy and Atomic Force Microscopy

3.1.1. Principle of the techniques

STM can image the topography of (semi)conductive samples by measuring the tunnelling current between the conductive tip and the sample when applying a voltage (**Figure 9A** (see details in [84]). In the last decade, STM has been applied to investigate the helical wrapping of self-assembled doxorubicin[85][86] and DNA[87] on single-walled CNTs. The physical adsorption of doxorubicin was related to the π-stacking between aromatic molecules and CNT benzene rings. As shown in **Figure 9C,** different conformations of the adsorbed doxorubicin have been revealed such as monomeric or dimeric molecules adsorbed in single-stranded or double-stranded structures. The resulting closely packed helical structures could be the reason of the high loading efficiency of CNTs for doxorubicin (up to 80-160%).

The need for conductive surfaces to allow the tunneling current represents the main drawback of STM. Conductive substrates are employed to analyze thin layers of organic and biological materials. In the previous examples, both CNTs and magnetoelectric NPs (upon application of a direct current magnetic field) behave as semi-conductive materials. For thicker specimens, metal coating or tagging is required to make them conductive. For instance, the structure of poly(amidoamine) dendrimers has been imaged using platinum and copper metal ion tagging allowing a spatial resolution down to 0.2 nm.[88]–[91]

In contrast to STM, AFM is suitable to characterize both conductive and insulating materials. The tip probes the local tip-surface interactions to map the sample topography and its physicochemical properties. A visible laser beam combined to a four-quadrant photodetector is used to detect the cantilever deflections related to the interactions (repulsive or attractive forces) with the sample surface during scanning (**Figure 9B**).

AFM imaging is mainly performed according to three modes: a static mode (contact mode) and two dynamic ones (non-contact and tapping modes). In the contact mode, the static tip touches the sample surface resulting in repulsive interactions. In the non-contact mode, the probe is slightly oscillating (~10 nm) at the vicinity of the sample surface without contact. In the tapping mode, also known as intermittent-contact mode, larger oscillation amplitudes (~200 nm) are applied. At each cantilever oscillation, the tip touches the sample and moves away.[92] In the contact mode, strong lateral forces and tip penetration occur and may damage both the tip and the sample, distort soft materials or sweep weakly bounded NPs. Conversely,

dynamic modes induce lower interaction forces and are more appropriate to preserve the integrity of sensitive materials such as organic NCs and biological materials. With these features, AFM has been applied since 1994 to determine the size and shape of NCs, such as biodegradable polymeric nanospheres of 90-150 nm,[93] and is now widely employed in the field of nanomedicine.[94]

Both STM and AFM have the advantage of a high-resolution imaging without complex sample preparation as the studied objects can be either directly synthesized (NPs) or grown (cells) onto the substrate, or deposited as a solid (powders and slices) or a drop of suspension. For poorly adhering NPs, a chemical coating can also be added onto the substrate. Sample preparation may lead to aggregates that may hamper individual analysis of particles. Hence, the dispersion and concentration of NPs has to be precisely controlled as well as their interactions with the substrate. Both STM and AFM are time-consuming techniques with an acquisition time increasing with the scanned area[92] which limits the number of objects accessible for analysis. Moreover, thermal drift may strongly affect the measurement for long acquisitions and restrain the observation of a large number of NPs hampering analysis statistics. At the opposite of EM, experiments can be carried out not only in vacuum but also in air or in liquid conditions. Nonetheless, air conditions require the sample drying to remove spurious interactions with humidity. If so, particular attention is needed regarding the alteration of the native morphology of hydrated NCs. Besides, since the signal results from short-range interactions, STM and AFM are only surface techniques and may not be representative for the whole volume of the sample. Extracting information on buried material is a hazardous goal that can only be reached in certain cases. The presence of drug inside NPs or NPs inside cells, changes the physicochemical properties of the sample surface and hence, the tip-surface interaction. Thus, their 2D location and distribution can be mapped with a high resolution. In AFM, the tapping mode not only preserves the integrity of the sample but also provides information on its nanomechanical properties. Upon contact, the sample viscoelasticity and adhesiveness induce energy dissipation that can be estimated by measuring the damping of the cantilever oscillation.[95] With this specificity, the AFM-tapping mode revealed the disk-like shape of prednisolone-loaded solid lipid NPs of approximately 200 nm and, by measuring the tip frequency changes, it suggested a soft shell surrounding the NPs.[96] Another study located cyclosporine-loaded PLGA NPs of ~280 nm in blood and liver after intravenous and *peroral* administration (**Figure 9D**) by the detection of the local increase of the tissue stiffness induced by the NPs.[97]

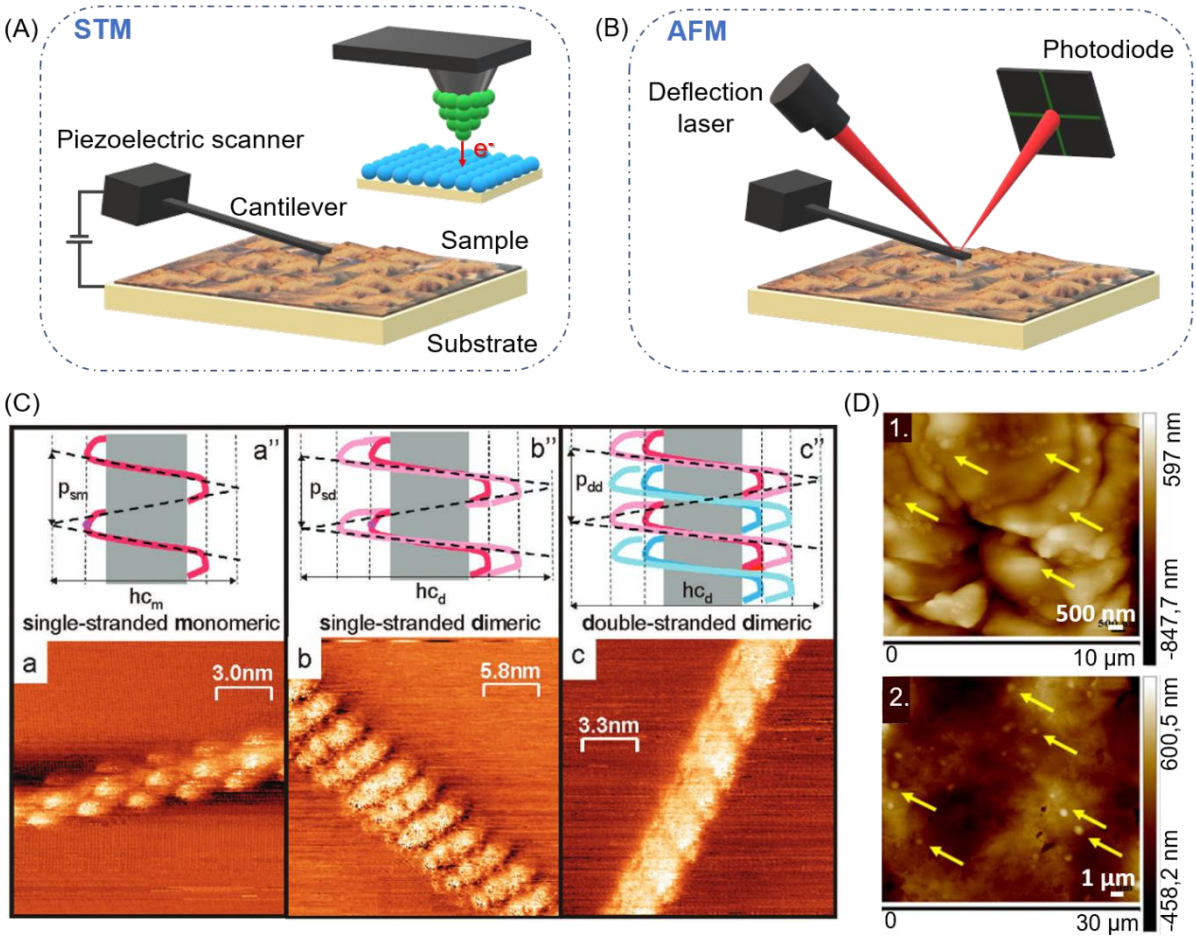

Figure 9. Schematic illustration of (A) a STM and (B) an AFM setup. Both are based on the scanning of a nanosized probe over the sample surface to measure the interactions. The probe consists of a cantilever ended by a sharp tip. A piezoelectric scanner allows 3D movements of the cantilever. STM probes the tunnelling current (red arrow) between the conductive tip and the (semi-)conductive sample. AFM measures the tip-sample force interaction. The system adjusts the cantilever position with respect to the laser deviations measured on the four-quadrant photodiode. (C) Schematic representations (top row) and STM images (bottom row) of the helical structures of doxorubicin self-assembled onto carbon nanotubes.[86] (D) AFM images of (1) rat blood and (2) liver tissue sections after intravenous administration of cyclosporine-loaded PLGA nanoparticles (indicated by yellow arrows).[97] (C) Adapted with permission.[86] Copyright 2017, Wiley-VCH. (D) Adapted under the terms and conditions of the Creative Commons Attribution License.[97] Copyright 2013, Public Library of Science.

3.1.2. AFM tip modifications

A variety of AFM technological developments were made, such as multiparametric, molecular recognition, multifrequency and high-speed imaging.[98] In particular, AFM tip has been modified to measure additional physicochemical properties of the sample surface. Electrostatic, magnetic, thermal interactions and chemical forces can be measured at the sample surface by coating or functionalizing the tip surface. With a metal coated-tip, the local variations of the electrostatic forces (Electrostatic force microscopy) or the work function (Kelvin probe force microscopy) can be mapped. Recently, Electrostatic force microscopy was applied to study the biosynthesis of bacterial cellulose-graphene oxide NPs which were further used to incorporate ibuprofen as a model drug.[99] Kelvin probe force microscopy was also employed to map the surface potential of gold nanorods during the removal of their surfactant.[100] Similarly, with a magnetic tip, Magnetic force microscopy measures the local magnetic field of the sample. With this approach, the electric properties of paclitaxel-loaded magnetoelectric NPs have been analyzed.[101] It has also enabled to monitor the cellular uptake of magnetic NPs in niosomes,[102][103] in human leukemia cells[104] and in human breast carcinoma epithelial cells.[105][106] Another strategy consists of functionalizing the AFM tip with NPs in order to investigate their interaction with biomaterials as done for lung epithelia cells in physiological fluid.[107] More recently, an AFM tip (diameter 20 nm) coated with serum proteins was used to mimic a NP in contact with blood and to directly examine its interactions with cells.[108] Note that this non-exhaustive list provides only few examples that highlight the growing interest of these approaches in the scientific community.

3.2.Optical near-field spectromicroscopies

By coupling AFM with optical spectroscopy, the so-called optical near-field spectromicroscopy reveals to be a multifunctional approach for simultaneous imaging and chemical analysis. Whereas conventional optical approaches are limited to a low spatial resolution of few hundreds of nanometers (Abbe diffraction limit), near-field techniques allow to drastically improve it down to tens of nanometers.

In the following sections, two techniques will be detailed: ***i)*** scattering-type Scanning Near-Field Optical Microscopy that probes the optical response of the sample, and ***ii)*** Photothermal Induced Resonance that measures the sample photothermal expansion. Both are able to simultaneously map the topography and the chemical information during the sample

scanning at a fixed wavelength or, alternatively, to acquire IR spectra at a specific location with the accuracy of AFM.

3.2.1. Scattering-type Scanning Near-Field Optical Microscopy

In the scattering-type Scanning Near-Field Optical Microscopy (s-SNOM), a laser beam is focused underneath the tip which operates both as a source and as a near-field detector: under illumination, it generates an evanescent wave (apex radius smaller than the wavelength) which locally interacts with the sample (**Figure 10A**). This leads to a resolution independent of the laser wavelength and only defined by the tip apex radius (~10nm). While scanning, the scattered light is analyzed by a spectrometer, producing amplitude and phase contrast images that are related to the local optical properties of the sample (reflective index and absorption).[109][110] Hence, s-SNOM is fully appropriated to highly scattering NPs such as gold. For instance, it has been applied to discriminate between 50 nm sized gold, silica and silica-capped gold NPs. Thanks to their high scattering response, gold NPs appear brighter in near-field amplitude images (**Figure 10B**). The presence of a gold core in silica-capped gold NPs also improved their scattering contrast (higher amplitude, red line in **Figure 10C**) as compared to bare silica NPs (blue line in **Figure 10C**).[111]

At last, s-SNOM is constrained by the same limitations regarding the sample drying in air conditions than AFM. Moreover, it suffers from its inability to image poorly scattered samples such as organic NCs and biomaterials. Nonetheless, by using metal-coated tips and more particularly plasmonic ones (gold or silver), its sensitivity may be improved according to the plasmon-enhanced spectroscopy effect.[112]

Tip-Enhanced Raman Scattering

Beyond a simple differentiation by dielectric mapping, s-SNOM fitted with the appropriate spectrometer is able to readily identify NCs components by measuring and mapping their specific molecular vibrational modes. This can be obtained by coupling either Raman or IR spectroscopy to the set-up.

When coupled with Raman spectroscopy, s-SNOM collects the light inelastically scattered by the sample and is known as Tip-Enhanced Raman Scattering (TERS). It allows a

nanoscale Raman spectroscopic imaging by employing a plasmonic metal-coated tip (gold or silver) to improve the weak Raman signal. More details on TERS can be found in Kurouski *et al.*[113]. Ashtikar *et al.*[114] used deuterated phospholipids as spectral markers to track liposomal systems of around 80 nm in human skin upon topical applications. The liposomal systems were detected in the topographic images, where a high density of flattened vesicular structures (50–300 nm diameter) were observed in the deep layers of the *stratum corneum*. The detection of the vibrational signature of the deuterated lipids (characteristic C-D band at 2170 cm^{-1}) enabled to ascertain that the liposomal formulations were intact inside the skin. Interestingly, TERS has also shown the presence of free deuterated-phospholipids.

Nano-FTIR spectroscopy

In the Fourier transform infrared nanospectroscopy (Nano-FTIR spectroscopy), s-SNOM is coupled with IR spectroscopy which uses an IR laser to illuminate the sample at its vibrational resonance. Broadband IR sources are generally employed to record the information over the complete IR spectral range since monochromatic lasers requires repeated scans at different wavelength involving time-consuming acquisitions, sample drift, tip wearing and finally measurement distortion.[115] Notably, synchrotron sources provide a high-power density in a wide spectral range, from 500 to 5000 cm^{-1}, particularly interesting since it includes the biological window (approximately from 530 to 1430 cm^{-1}). With this approach, the interactions between antimicrobial NPs and *Escherichia coli* bacteria were investigated by Capeletti *et al.*[116] In this study, carbohydrate-coated silica NPs of around 100 nm were designed to target the membrane of gram-negative bacteria. **Figure 10D** shows that, in agreement with topographic data, the characteristic bands of NP silica and amide from membrane proteins are only detected together at the NP-bacteria interface (purple areas in Figure 10D). These results also reveal shifts of the amide bands related to a hydrogen bonding between the NPs and the bacteria membrane.

In a nutshell, TERS and Nano-FTIR spectroscopy (s-SNOM) are powerful techniques to characterize NPs from their optical response. However, the sample drying, applied to minimize the water interactions and its IR absorption, might also distort the NC's native structure. Besides, as the near-field signal results from the detection evanescent waves, shallow buried materials can only be analyzed in a limited depth close to the specimen surface. It has also to be mentioned that s-SNOM is poorly reproducible. The near-field signal

depends on the tip-sample interaction and on the acquisition conditions such as the scanning mode and the tip nature and geometry, which can affect the measurement. The acquired spectra can be quite different from the one obtained by conventional far-field techniques.

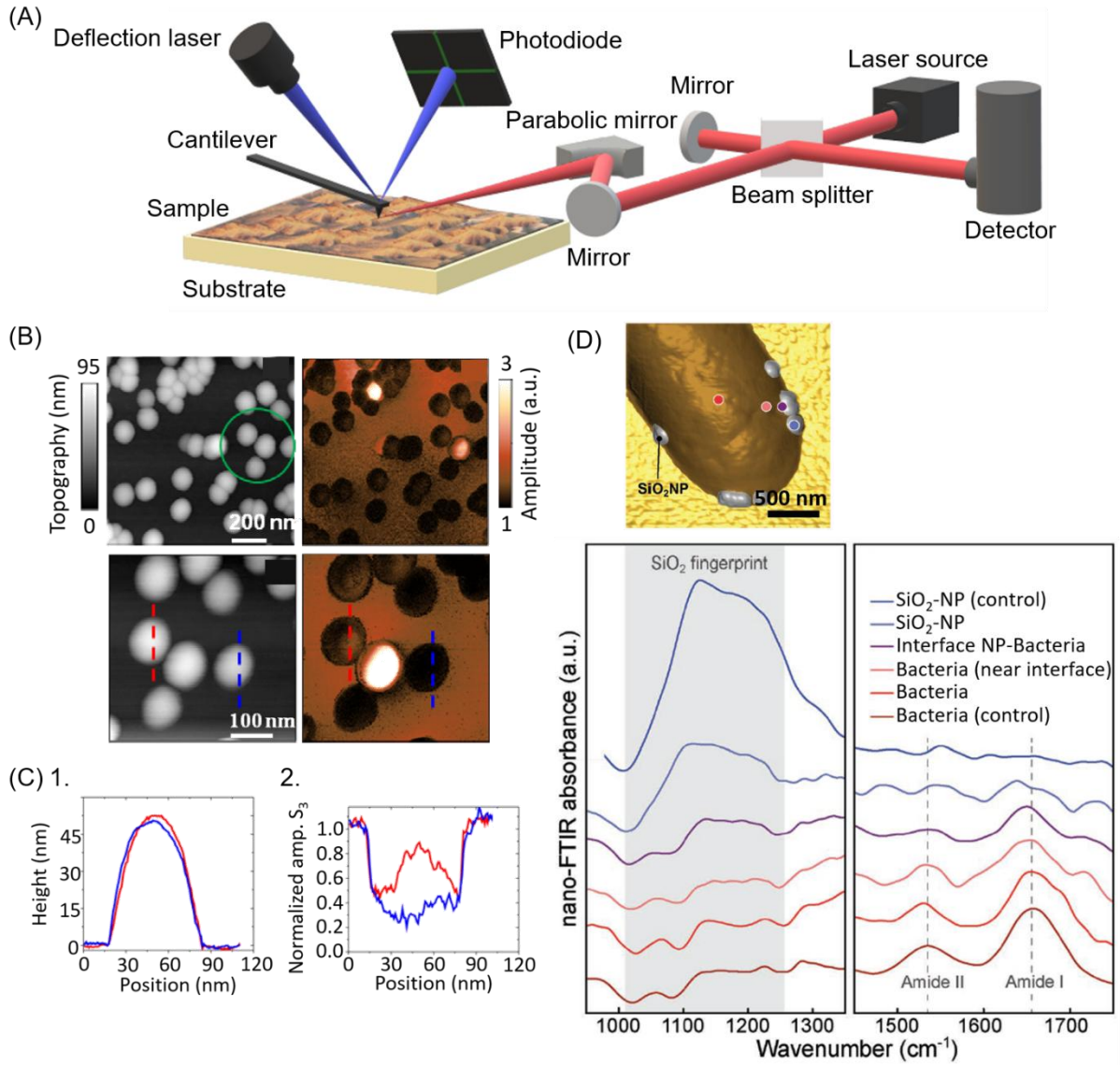

Figure 10. Scattering-type scanning near field optical microscopies: (A) Schematic illustration of ~~a~~an s-SNOM setup. While a sharp tip is scanned over the sample, a focused light source (visible or IR, monochromatic or broadband) locally illuminates the surface. The detector collects the sample optical response. (B) Topographic and s-SNOM amplitude images of gold, silica and silica-capped gold NPs. Gold NPs appear as brightest in near-field amplitude images due to their larger scattering response. The selected region of interest is indicated in green.[111] (C) Topographic (1.) and amplitude signal (2.) line profiles of the two silica and silica-capped gold NPs shown respectively in red and blue dashed lines in (B). The gold core improves the scattering contrast of the silica coating layer.[111] (D) Topographic image of a bacterium incubated with gluconamide-functionalized silica NPs (SiO_2-NP) and nano-FTIR spectra of corresponding regions. The redshift of amide I and blueshift of amide II spectral bands indicate the NP-bacterium interaction.[116] (B-C) Reproduced with

permission.[111] Copyright 2011, Optical Society of America. (D) Adapted with permission.[116] Copyright 2019, Wiley-VCH.

3.2.2. Photothermal-induced Resonances

Photothermal Induced Resonances (PTIR) (also named Atomic Force Microscopy-based Infrared, AFM-IR) combines AFM with IR spectroscopy to map the molecular IR absorption at a nanoscale resolution.[117] A pulse tunable IR laser locally illuminates the sample to excite molecules at their specific absorption wavelength (**Figure 11A**). Their non-radiative relaxation generates a local heating and a fast thermal expansion that is detected by the AFM cantilever. The recorded signal is then related to spectroscopic data and is similar to conventional FTIR.[113][118]

Drug and shell location in NCs

As in AFM, the PTIR-tapping mode is recommended for sensitive samples. As shown in **Figure 11B**, Mathurin *et al.*[119] have compared the effects of contact and tapping modes on PLGA NPs of 100-200 nm loaded with pipemidic acid (PIP). The tapping mode not only allows the observation of the specific core-shell structure of the PLGA NPs, but the 10 nm-resolution achieved also enables determining the drug distribution within NCs. Besides, in spite of the low amount of loaded drug (< 1 wt%), it is readily detected in the corona of the NCs (**Figure 11 C-D**). This location was well correlated with the fast ("burst") release of the drug.

More recently, chemical maps of 80 nm-sized cytarabine-loaded liposomes (**Figure 12E**) revealed the location of the drug in the NC's core. The drug location also affects the local nanomechanical properties of the liposome producing a contrast visible on the frequency maps: in **Figure 12F**, the liposome central region appears harder than its periphery in agreement with the drug distribution.[120] Besides, this study highlights the main limitation of the technique: the sample drying. Due to the osmotic pressure, the native morphology of the liposomes was affected inducing a shape change from spherical to ellipsoidal and a size increase from 80 nm to 100-200 nm. Note that the drying step could also influence the drug distribution within the NCs as the dehydration can induce the drug crystallization. To avoid crystallization upon drying, another study included a sucrose solution in the formulation of 97-130 nm-sized liposomes containing ciprofloxacin. Then, PTIR enabled to distinguish the

crystalline drug from its dissolved form according to the IR signal of the ionized carboxyl groups. The results were compared to cryo-TEM and AFM nanomechanical imaging where a uniform distribution was detected for the liquid drug whereas the crystalline form was located in the center of the liposomes.[121]

Several other studies emphasize the high sensitivity of plasmon-enhanced PTIR where a polarized IR beam was used to determine the geometry and molecular orientation of drugs immobilized onto gold and silver NPs, such as a selective Y5 receptor antagonist,[122] α-methyl-DL-tryptophan,[123] erlotinib[124][125] and nocodazole.[126]

Detecting NCs in cells and tissues

PTIR also rises a significant interest for mapping organic NPs within cells. Pioneering studies by Pancani *et al.*[127] allowed tracking 170 nm biodegradable poly(lactic acid) (PLA) NPs inside macrophages avoiding the need of labelling. The intense ν(C=O) stretching vibration band of the PLA NPs was used as a fingerprint (**Figure 11G**) and correlative microscopies ascertained that practically all the NPs were detected with a spatial resolution of approximately 10 nm (**Figure 11G** and **Figure 11H)**. More recently, Kemel *et al.*[128] investigated the penetration of Janus NPs (~150-300 nm) in human skin with a sub-100 nm spatial resolution. After a 24 h cutaneous application and vertical sectioning of the skin, a NP gradient was observed from the surface into the deepest layers of the *stratum corneum*.

These examples illustrate the capacity of PTIR to characterize NC interactions with drugs and biomaterials. However, it is constrained by two main limitations. First, as already mentioned, samples are usually dried to prevent from water spurious interactions and IR absorption. This significantly limits *in situ* experiments that are needed to analyze hydrated NPs and determine biological processes. Secondly, it is difficult to estimate the sample depth from which the signal is recorded. Hence, it is not possible to distinguish materials buried at different penetration depth (for example, NPs embedded in tissues).

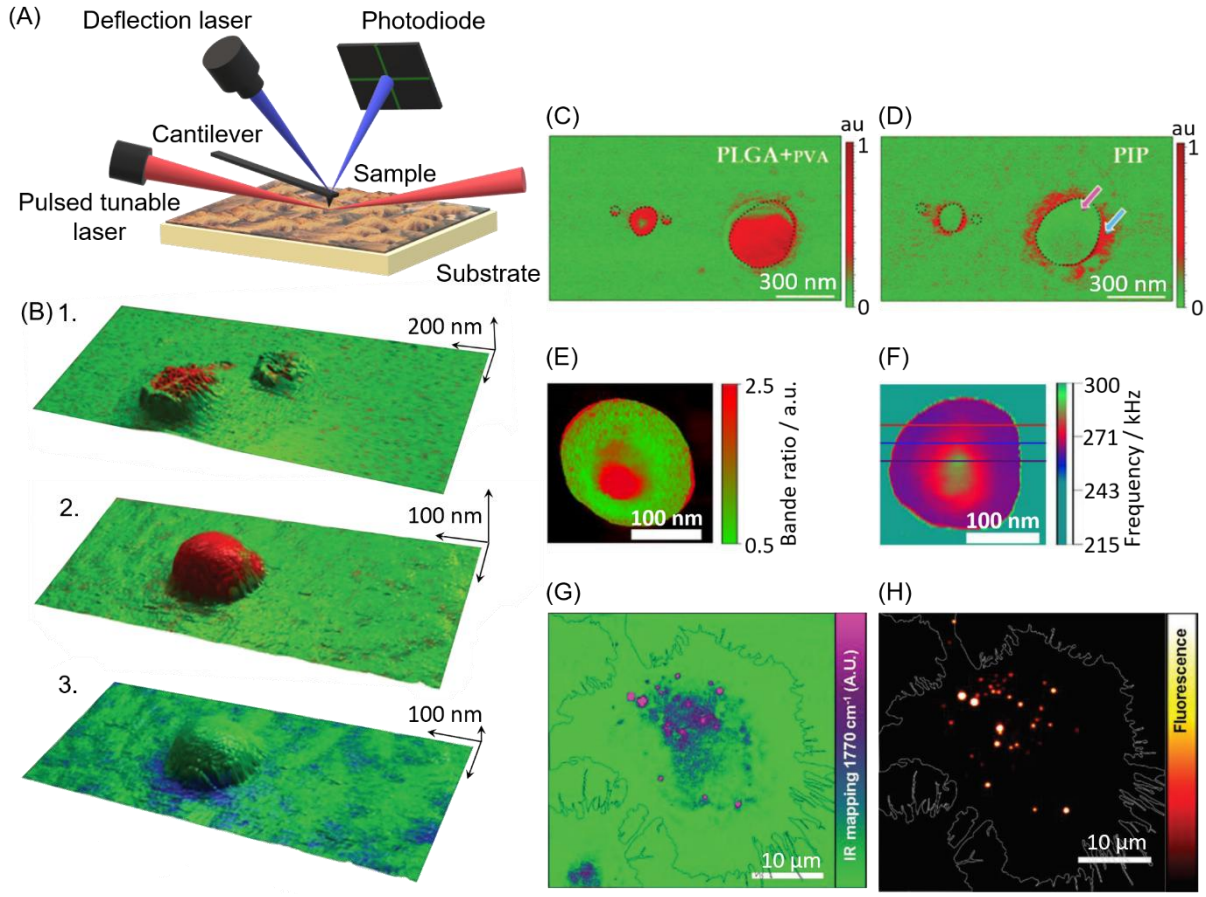

Figure 11. Photothermal Induced Resonances: (A) Schematic illustration of a PTIR setup. An IR laser illuminates the sample and induces a fast thermal expansion. The sample IR absorption is then deduced from the AFM cantilever deflection. (B) Overlay of topographic and chemical maps for PLA NPs in contact (1.) and tapping (2.-3.) modes. Red and blue color represent respectively the PLA C=O stretching vibration at 1760 cm^{-1} and the polyvinyl alcohol surfactant C-H bending vibration at 1415 cm^{-1}. The comparison highlights the damages induced in contact mode. (C-D) Chemical maps in tapping mode of PIP-loaded PLGA NPs at: (C) 1425 cm^{-1} (PLGA C-H vibration band) and (D) 1640 cm^{-1} (PIP C=O stretching vibration band). The co-location of PIP and polyvinyl alcohol is clearly visible in the NP shell (cyan arrow) around the PLGA core (pink arrow).[119] (E) Chemical map of cytarabine-loaded liposomes, obtained in contact mode, at 1528 cm^{-1} (pyrimidines C=N and C=C vibrations) and 1734 cm^{-1} (lipids C=O stretch vibration). The ratio between the two bands displays red and green colors corresponding to cytarabine rich and lipid rich regions, respectively. (F) Frequency map of cytarabine-loaded liposomes showing a stiffer region in the center related to the encapsulated drug.[120] (G) Chemical map and (H) fluorescence images of internalized Rho-PLA NPs in a THP-1 macrophage acquired with a PTIR laser at 1770 cm^{-1} (PLGA ester groups) and a confocal microscope, respectively.[127] (B-D) Adapted with permission.[119] Copyright 2018, Royal Society of Chemistry. (E-F) Adapted with permission.[120] Copyright 2019, Springer Nature. (G-H) Adapted with permission.[127] Copyright 2018, Wiley-VCH.

4. Single particle analysis in suspension

Dynamic Light Scattering (DLS) is the most common method to determine the size distribution of NPs in their native environment in solution. As shown in **Figure 12A-i**, it consists of a polarized laser that illuminates the sample and of a photodiode that collects the light scattered by NPs. The NP hydrodynamic radius is determined from the diffusion coefficient provided by the Stokes-Einstein equation.[129] Nevertheless, only an averaged size can be measured. As an alternative, three techniques able to provide the size and size distribution of individual particles in suspension are discussed here: Nanoparticle Tracking Analysis, Single Particle Extinction and Scattering, and Tunable Resistive Pulse Sensing.

4.1.Nanoparticle Tracking Analysis

Nanoparticle tracking analysis (NTA) analyzes the Brownian motion of the individual NPs in suspension providing both the NP concentration and their size distribution. The sample is illuminated with a laser at a low incidence angle and the scattered light emitted by each NP is collected with an optical microscope fitted with a camera (**Figure 12B-ii**). Each NP appears as a bright spot and its trajectory allows to determine its diffusion coefficient and then, its hydrodynamic radius. The size distribution can be unambiguously determined for NPs larger than 50 nm but this limitation can be lowered down to 15 nm for high refractive index NPs, such as gold particles.[130][131] The NP concentration can be determined, in a range typically from 10^6 to 10^9 particles *per* mL. In addition, with an appropriate experimental design, NTA may advantageously be used to characterize the size and concentration of NPs intrinsically fluorescent or after labelling.

Filipe *et al.*[132] have compared the ability of DLS and NTA to determine the size distribution of several monodisperse or polydisperse NP samples. Whereas DLS measurements were strongly affected by the presence of large particles, NTA provided a better size accuracy for polydisperse PLGA NPs thanks to its individual detection (**Figure 13A**). However, as shown in **Figure 13B,** NTA was limited by its inability to detect sizes smaller than 30 nm, such as insulin monomers and sucrose molecules from the buffer. Other disadvantages, shared with DLS, are the need for a stable suspension to avoid sedimentation during measurements and the inability to analyze particles in complex media (for example in the presence of proteins and aggregates) due to the scattering background arising from the other materials in the suspension.

4.2.Single Particle Extinction and Scattering

Although not widely used in drug NC investigations, Single Particle Extinction and Scattering (SPES) is an interesting approach to analyze polydisperse samples and suspensions in complex media. Particles in suspension pass through a flow cell with a laminar flow at a constant speed, under a laser beam illumination (**Figure 12C-iii**). The transmitted and scattered fields are both collected by a photodiode and superimposed to produce interference patterns allowing the measurement of the particle diameter and refractive index.[133]

The major advantage of SPES is its to distinguish NCs with different compositions within the analyzed sample. The evolution of the size distribution of PLGA and model polystyrene (PS) NPs has been studied in complex biological media and the results were compared with DLS.[133][134] While DLS is limited by the scattering background raising from biological materials, SPES enables to distinguish the NPs from the to monitor the degradation of PLGA NPs in phosphate buffered saline[133] and the protein corona formation around PS NPs incubated in murine serum, filtered and unfiltered murine blood.[134] In addition to size determination, Potenza *et al*.[135] have demonstrated the possibility to distinguish plasmonic metal NPs with different shapes. The NP morphology (shape and size) affects its plasmonic properties and, consequently, its optical properties. For a sample composed of mixed spherical and branched NPs, in a comparable size range, the plotting of the real (reflective index, Re S(0)) and imaginary part (absorption, Im S(0)) of the scattering field reveals the optical responses of each fraction (**Figure 13C**) and so, the size dispersion of the sample, from which the different populations can be identified.

4.3.Tunable Resistive Pulse Sensing

Tunable Resistive Pulse Sensing (TRPS) is a versatile technique to measure the size, shape and surface charge of individual NPs and their concentration. The NPs are suspended in an electrolyte and placed in a cell separated in two parts by an elastomeric single-nanopore membrane. By applying voltage and pressure, the NPs are driven to pass one by one through the nanopore resulting in an ionic current. At each particle crossing occurs a current blockade event (resistive pulses) whose magnitude, duration and frequency are measured to determine the particle size, surface charge and concentration, respectively (**Figure 12D-iv**). The nanopore size is tunable by membrane stretching or relaxation. Although it provides several dynamic size ranges from 40 nm to tens of micrometers to fit with the sample, TRPS is not

appropriate for highly polydisperse NPs and excludes the detection of small ones (< 40nm). Besides, very low concentrations are necessary for the NPs to pass individually through the nanopore and high ionic strength are required. These conditions might lead to artefacts and a misrepresentation of the sample in its native environment.[136]

Sikora *et al.*[137] have compared TRPS with DLS, Differential Centrifugal Sedimentation (DCS) and Electrophoretic Light Scattering (ELS) for the study of the protein shell formation around silica NPs. They monitored the size and surface charge evolution of plain and aminated silica NPs incubated in tris(hydroxymethyl)aminomethane buffer and serum solution. While DLS overestimates the NP sizes due to the presence of aggregates in serum, DCS requires density information on the protein coating to determine its thickness. In contrast, TRPS successfully revealed the formation of a 5 nm sized-protein shell (**Figure 13D**). This coating was corroborated by the increase of the NP surface charge. The TRPS results were similar to the ELS ones.

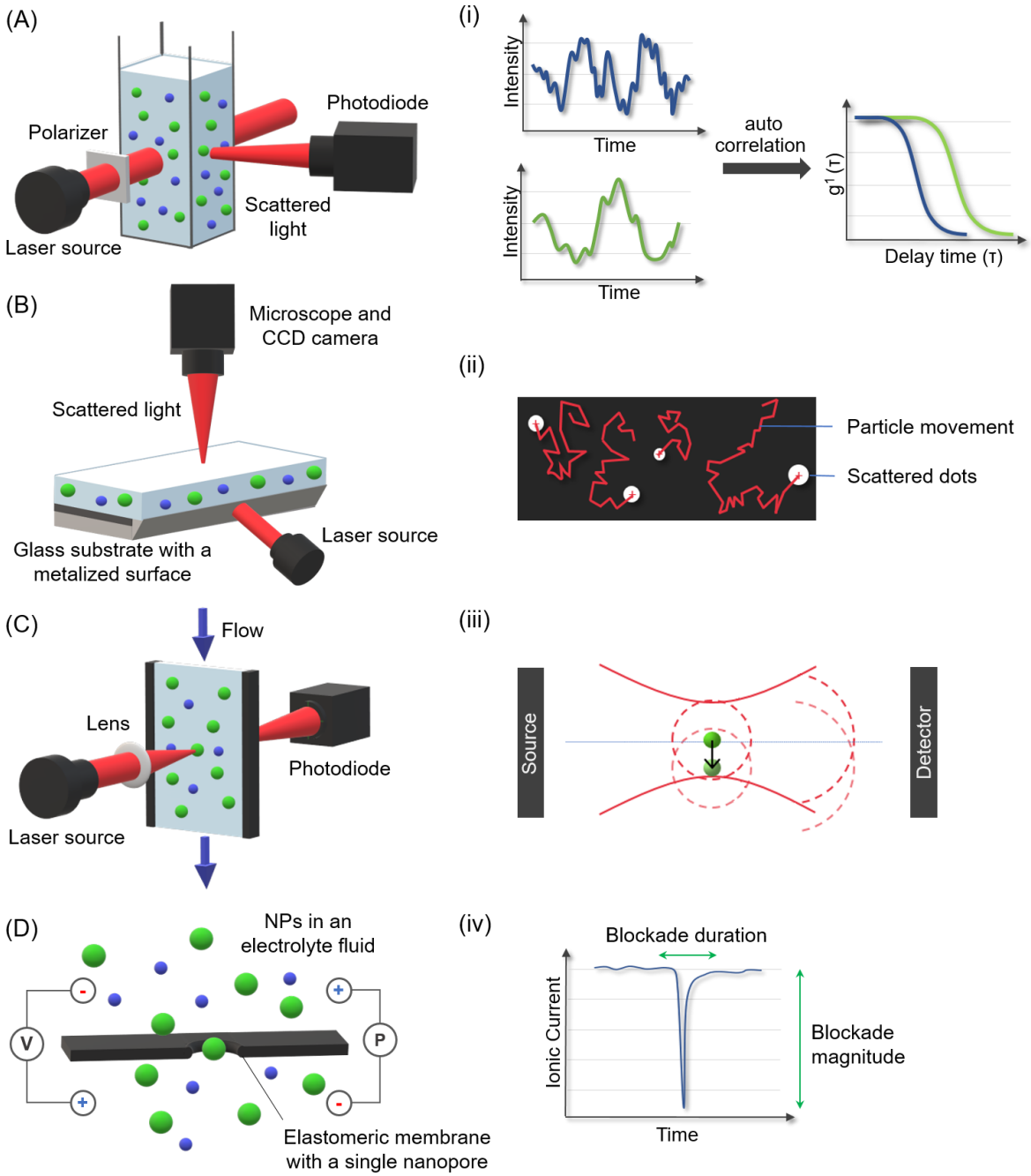

Figure 12. Schematic illustrations of approaches for Single particle analysis in suspension: Dynamic Light Scattering (A), Nanoparticle Tracking Analysis (B), Single Particle Extinction and Scattering (C), Tunable Resistive Pulse Sensing (D) techniques and their respective signals (i-iv). (A) DLS provides the mean diameter and size distribution of NPs. A polarized laser beam illuminates the sample and a photodiode collects the scattered light. (i) The intensity fluctuations are related to the Brownian motion allowing the determination of NPs hydrodynamic radius. (B) NTA measures the size of individual NPs by tracking their Brownian motion. The sample is illuminated by a laser beam through a prism-edge optical substrate and an optical microscope allows the visualization of the trajectories of individual NPs which appear as bright spots by scattering light. (ii) The NP hydrodynamic diameter is determined from their diffusion coefficients. (C) SPES determines the diameter and refractive index of single NPs. A laser beam is focused into a flow cell where particles in suspension are driven by a laminar flow a constant speed. Each particle passes through the focal plane producing a scattered field. (iii) The transmitted and scattered fields are collected by a

quadrant detector and generate time-dependent interferences whose intensity fluctuations are related to the extinction cross section and the sizes of individual particles. (D) TRPS determines single NP size and surface charge. The NPs are suspended in an electrolyte and forced to pass one by one through a membrane which has a single well calibrated nanopore. A voltage is applied across the membrane, and the passage of individual NPs through the nanopore generates current blockage events resulting in a signal (iv) whose intensity and duration are characteristic of the NP size and charge. The blockage frequency is related to the sample concentration.

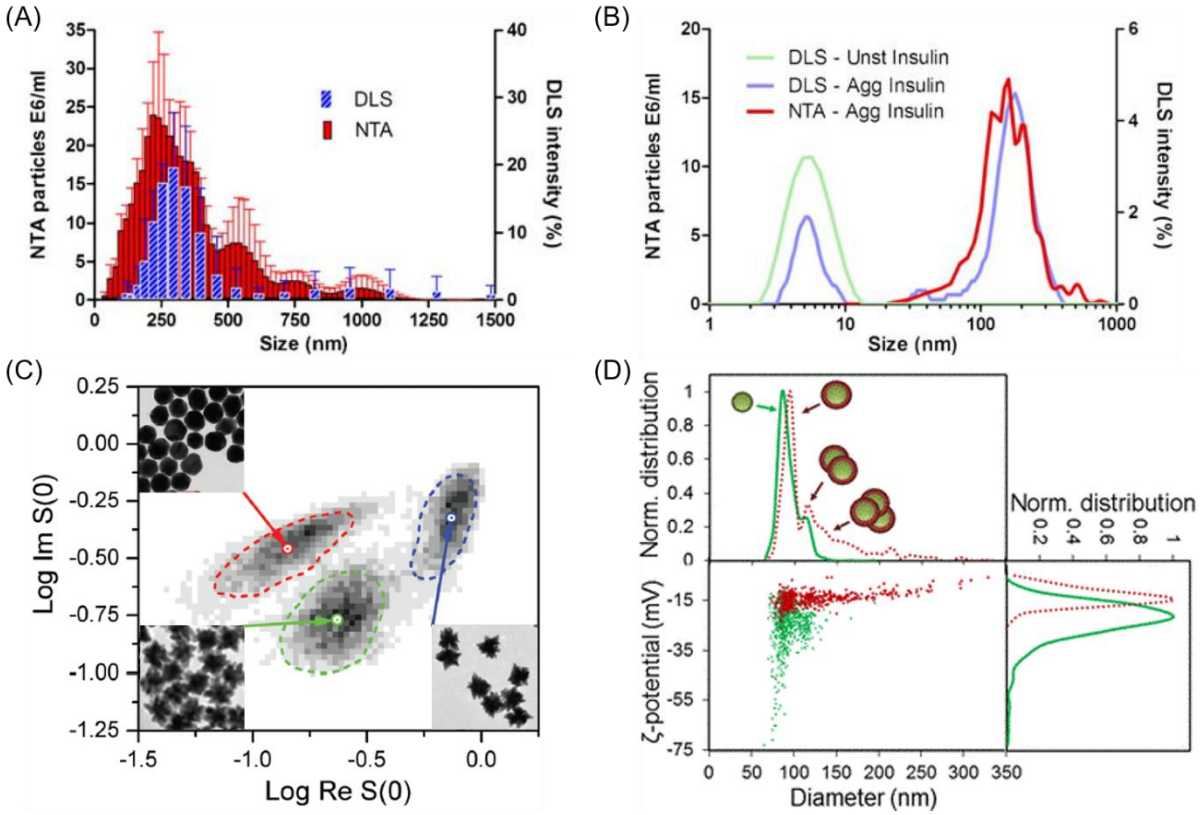

Figure 13. Examples of DLS, NTA and TRPS analysis: Size distribution of (A) PLGA NPs and (B) insulin aggregates ("Agg") measured with DLS (blue) and NTA (red). "Unst" stands for unstressed insulin that is present in solution as monomers (green).[132] (C) Histogram of the real (Re S(0)) and imaginary (Im S(0)) parts of the scattered field of mixed spherical (80nm in red) and branched gold NPs (60 nm in green and 124 nm in blue) measured with SPES. The different populations are quantitatively identified from their different optical response. The corresponding TEM images are shown in the insets. The grey tones indicate the number of particles for a given value of Re S(0) and Im S(0) (in Log scale).[135] (D) Size and ζ-potential distributions of silica NPs uncoated (green) or coated with a protein layer (red) measured by TRPS. "Norm." stands for normalized distributions, calculated from the measurements of ζ-potential and sizes of individual NPs.[137] (A-B) Adapted under the terms and conditions of the Creative Commons Attribution Non commercial License.[132] Copyright 2010, Springer Nature. (C) Adapted under the terms and conditions of the Creative Commons Attribution 3.0 Unported Licence.[135] Copyright 2017, Royal Society of Chemistry. (D) Adapted under the terms and conditions of the Creative Commons Attribution 3.0 Unported Licence.[137] Copyright 2016, American Chemical Society.

5. Other approaches

5.1. Nanoscale Secondary Ion Mass Spectrometry

Nanoscale Secondary Ion Mass Spectrometry (nanoSIMS) is a highly sensitive analytical approach (detection limit of the order of parts-per-billion) based on the analysis of the secondary ions generated by the sputtering of the sample surface by a focused primary ion beam.[138] Ion impact energy is about few keV and can be adjusted depending on the depth of interest and spatial resolution reaches values down to 50 nm. For each position of the beam, the secondary ions are then analyzed by a mass spectrometer allowing the identification and the mapping of the different elements constituting the specimen. It is particularly interesting to mention that isotopes can also be identified offering the possibility of an isotope labelling. In addition, the specimen surface can be imaged by detecting the emitted secondary electrons like in a SEM.

Proetto *et al.*[139] took advantage of the capabilities of nanoSIMS to discriminate between different isotopes to investigate the cellular uptake of drug-loaded polymeric NPs. The two labels (^{195}Pt from the anticancer drug oxaliplatin and ^{15}N from the polymer) were detectable by nanoSIMS and were used to determine the NPs location after their incubation with cancer HeLa cells. Surface morphological features of HeLa cells were observed *via* a secondary electron image that was overlaid with the enriched ^{195}Pt and ^{15}N maps obtained from nanoSIMS. The 3D localization of the NPs was determined by eroding the cell with the beam and by acquiring maps of ions coming from different depths within the cell. The co-localization of ^{195}Pt and ^{15}N signals provided a clear evidence that the internalized NCs were intact (**Figure 14A**). However, after 24h incubation with the cells, the slight decrease of the ^{15}N as compared to the ^{195}Pt suggested that the drug was released out of the NCs (**Figure 14B**).

Polymeric NCs loaded with ^{13}C-labelled resveratrol and tiny magnetite NPs were studied by nanoSIMS to determine their interaction with cells.[140] Tracking of both labels (^{13}C from the drug and Fe from magnetite) enabled assessing the fate of the NCs, which were targeted efficiently to macrophages and astrocytes to exert a protective effect after neuronal injury.

In another study, multifunctional NPs were made of 60 nm Raman-active gold cores covered by a monolayer of Raman-active dye and surrounded by a 30 nm thick silica shell.[141] Their location in human macrophages was analyzed both by SEM and nanoSIMS. Fewer NPs were detected by nanoSIMS due to its lower spatial resolution as compared to SEM. Moreover, this study underlines the low depth of penetration of nanoSIMS: NPs deeper than 1-2 nm from the surface were not detected because ion generation and sputtering only occurred in a very reduced volume.

More recently, SIMS has been coupled with time-of-flight secondary ion mass spectrometry (ToF-SIMS) for the detection of coatings on NPs[142] and the biomolecular imaging of NP-cell interactions[143] representing a valuable tool in nanotoxicology.

NanoSIMS is a method of choice to analyze trace elements, but this approach is not able to detect changes in speciation and obtaining quantitative information is an arduous task because the yields of secondary ions are different for each investigated element and are influenced by their environment. As for the electron microscopies depicted here, SIMS is operated under high vacuum and requires sample dehydration and embedding (see paragraphs 2.1.1 and 2.1.2).

5.2. Synchrotron based-X-ray spectromicroscopies

Synchrotron based-X-ray spectromicroscopies constitute highly sensitive and rather non-destructive approaches allowing to image and to map quantitatively the chemical composition (including trace elements) at a sub-micron resolution. The description of the principles and analytical capabilities of this huge panel of approaches goes beyond the scope of the present review which will focus on a few examples to illustrate the interest and limitations of these techniques for NC studies.

The X-ray energies define the current capabilities and impose the specific instrumental constraints of each approach. The first limitation comes from the attenuation length that determines the provided information and the specimen preparation. Hard X-rays (above 5 keV) are able to penetrate deeper and even to pass through macroscopic specimens. This deep penetration has been exploited to image large specimens without the need of sectioning, as whole cells[144][145][146] or complete small animals, including live ones.[147][148] Despite their advantages, hard X-ray spectromicroscopies are not only limited to a low spatial resolution (~

1 µm), not enough to resolve individual NPs, but also to a low spectral resolution that restricts the analysis to elemental characterization. Conversely, even though soft X-ray (from 50 to 3000 eV approximately) penetrations are limited to the micron range they offer the advantage of a high spatial resolution (~20 nm) and a very high spectral resolution compatible with compound identification. Besides they are particularly well adapted to organic and biological specimens because of their energy that gives access to the edges of the light elements composing these systems

X-ray spectroscopic information can be obtained from two techniques: X-ray fluorescence spectroscopy (XRF) that detects the X-ray fluorescence from the specimen when irradiated with a fixed X-ray incident energy and X-ray absorption spectroscopy (XAS) that determines the absorption coefficient of a fixed electronic edge as a function of incident energy. XAS gives access to the full speciation of the specimen by examining the fine structures of the absorption edges (the so-called X-ray absorption near edge structures, XANES, also called near edge X-ray absorption fine structure, NEXAFS). The data obtained from XANES measurements are very similar to EELS spectra and can be directly compared. XRF and XAS can be combined to access to the elemental composition and chemical speciation.

Interestingly, X-ray spectromicroscopies are not constrained to the analysis of fixed or dried samples in vacuum, since experiments can also be carried out on wet samples under atmospheric pressure (helium) which is an advantage for biological systems. X-ray approaches are rather non-destructive but for sensitive samples, low-dose imaging and cryogenic conditions are in many cases recommended (see paragraph 2.1.2).

5.2.1. 2D imaging

Like electron microscopes, X-ray imaging relies on different setups based on full-field (Transmission X-ray Microscopy, TXM) or scanned (Scanning Transmission X-ray Microscopy, STXM) modes. This latter mode is particularly well adapted to image the NC distributions within cells due to its high spatial resolution (down to 20 nm approximately). The incident energy beam is usually adjusted in the spectral region bounded by the carbon and oxygen K-edges (284–540 eV), the so-called “water window”, in order to enhance the contrast of organic compounds so that biological specimens and their interaction with NCs

can be studied without staining nor labelling. Then, specimen images are obtained from the detection of the transmitted X-rays, or of the X-ray fluorescence or photoelectrons secondary emitted when the specimen is illuminated by the primary X-ray beam.[147][149]–[151]

In Graf *et al.*[152], soft-STXM was employed to investigate at a 40 nm resolution the penetration of core-shell (silica-gold and gold-silica) NPs (sizes ~ 100-300 nm) into human skin after ultramicrotome sectioning. Compared to TEM that is limited to ultrathin section, STXM has the advantage to be usable on thicker sections (500 nm) compatible with the largest studied NPs (300 nm). However, the smallest ones (94 nm total diameter with 49 nm gold core) were at the STXM resolution limit and they were only detectable by carrying out and comparing measurements at different photon energies (below the C 1s and at the O 1s edges). More recently, Graf *et al.*[153] have combined cryo-SEM, EDX and soft-STXM to assess the penetration of gold nanospheres (80 nm) and nanorods (250 nm) on 3-5 µm sections of human skin prepared by plunge freezing and freeze drying.

The coupling of STXM with XRF or XAS is well appropriated for spectroscopic analysis at high spatial resolution. Two acquisition modes are then possible: chemical spectra can be obtained at a fixed specimen position over a wide energy range or chemical maps can be acquired by scanning the specimen across the beam position at a fixed energy. The latter mode is rather time consuming because it requires several scans at different energies to cover the full energy range of the absorption edge. Despite the high resolution of these approaches, to date, most of the NC studies only concern their distributions and do not characterize individual NPs. For instance, soft-STXM was combined with XRF in several studies analyzing the internalization and toxicity of single-walled CNTs (from 5 nm to 1000 nm in length in cervical epithelial cells,[154] mesothelial cells[155] and human choriocarcinoma.[156] Another study determined the distribution of cobalt ferrite NPs (~ 35 nm) and assessed their elemental modification (Fe to Co ratio) occurring in mouse fibroblasts.[157] Their chemical degradation (accumulation of Co) were related to changes in the cellular morphology and potentially contributed to the cell death. Gianoncelli and coworkers investigated the distribution and potential toxicity of magnetic NPs (Fe_2O_3 and $CoFe_2O_4$) of approximately 35 nm and 110 nm incubated with human glioblastoma-astrocytoma cells, with a spatial resolution of 650 nm (**Figure 14C**).[158] Interestingly, a quantitative study reported the investigation of the cellular uptake and toxicity of 30 nm sized luminescent silica NPs. Their distribution within human adenocarcinoma cells were mapped with a spatial resolution of 500

nm and the NP average concentration was estimated between $2.04 \times 10^6/\mu m^3$ and $2.22 \times 10^6/\mu m^3$ per cell volume.[159]

When coupled to soft-STXM, XANES not only provides the distributions of the chemical species composing the sample but also a fine analysis with the aim of investigating the chemical changes induced by cell interactions. For instance, it was applied to track the uptake and bioaccumulation of TiO_2 NPs with different hydrodynamic sizes into epithelial cells of Daphnia magna gut.[160] An in-depth study of the biodistribution and biomodification of iron oxide NPs (~130 nm) of different crystalline phases was performed in the digestive tract of Daphnia magna. The evolution of the XANES spectra on the Fe L-edge revealed the biomodification (oxidative dissolution) of the Fe_3O_4 NPs.[161] In another study, Yamamoto *et al.*[162] quantitatively monitored the penetration of organic core-multishell NCs of 10 nm after topical application on human skin and the release of their dexamethasone drug content. With a fine analysis of the oxygen spectroscopic signature, XANES enabled to detect 5% drug loading in NCs and revealed that NCs remained in the *stratum corneum* even after 1 000 min exposure.

As already mentioned, studies based on hard X-ray suffer from their low spatial resolution. However, the X-ray focusing systems has been recently improved leading to sub-micron probes.[163] Alternatively, ptychography, a coherent diffraction imaging approach, allows nanometer resolution in cellular maps, including for trace elements.[164] Ptychography uses a STXM setup to record a set of diffraction patterns from the successive illumination of overlapping regions on the sample. An iterative algorithm is then used to reconstruct a 2D image with an amplitude and phase contrast. By coupling XFR with ptychography, Stachnik *et al.*[165] have mapped quantitatively the distribution of antibiotic loaded-iron oxide NCs within macrophages, simultaneously with the identification of the different sub-cellular structures, with a spatial resolution below 100 nm.

5.2.2. 3D imaging by Synchrotron X-ray tomography

As described for electron tomography (see paragraph 2.1.3.), X-ray tomography is based on the acquisition and processing of a series of 2D X-ray images from the sample recorded at different orientations. to get a 3D image. In Yao *et al.*[166], two tilted series were acquired by STXM at two energies below and above the absorption edge of a specific element (Dual-energy contrast X-ray microscopy) to quantitatively map the 3D distribution of

antitumoral $Gd@C_{82}(OH)_{22}$ NPs inside macrophages, with a spatial resolution of 80 nm. The NPs were mainly found in an aggregated state within phagosomes. A high spatial resolution (16.5 nm) was achieved when localizing Fe_3O_4-SiO_2 NPs within HeLa cells, by combining X-ray tomography with ptychography. The high spectral sensitivity of the technique also revealed distinct oxidative states which may result from the natural oxidation of Fe_3O_4 during storage.[167]

Another possible approach, cryo-soft X-ray Tomography (cryo-SXT), lies in the acquisition of tilted series of soft X-ray transmission microscopy images on cryo-specimens giving access to a full 3D volume at resolutions down to 25 nm.[168] Cryo-SXT exploits the property of soft X-rays in the water-window region which are strongly adsorbed by the carbon-rich structures composing the biological specimens whilst their attenuation by ice is minimal. It is the only imaging approach able to provide 3D maps at high resolution of unstained vitrified whole-cells, thus avoiding chemical treatments and sectioning. It was employed to study the cellular uptake and distribution of gold NP within fibroblasts and macrophages.[169] Recently, Kepsutlu *et al.*[170] investigated the uptake of dendritic polyglycerol sulfate-coated gold NPs in human lung epithelial cells. Cryo-SXT was able to detect gold NPs in specific cellular localizations (cytoplasm and lipid droplets) at levels undetectable by confocal light microscopy. Another study assessed the distribution and cytotoxicity of cisplatin-coated gold NPs of tens of nanometers within cutaneous squamous cell carcinoma. In this study, contrary to TEM, cryo-STX enabled to discriminate the different organelles and to visualize the internalized NPs in the perinuclear region. The NPs were found to enhance the cisplatin delivery inside cancer cells, but did not penetrate inside nucleus.[171] Interestingly, Reineck *et al.*[172] correlated cryo-SXT with confocal fluorescence microscopy, SEM and AFM to monitor the uptake mechanism of fluorescent nanodiamonds inside and on the surface of cancer cells with a spatial resolution of 28 nm. Moreover, cryo-specimens employed in cryo-SXT are compatible with correlative cryo-epifluorescence microscopy and TEM. By combining cryo-SXT with these two techniques, Chiappi *et al.*[173] investigated the interaction of 15 nm-sized SPIONs with breast cancer cells, at a spatial resolution of 60 nm. More recently, correlative cryo-epifluorescence microscopy and cryo-SXT were employed to visualize the cellular uptake of plasmid DNA-loaded MOFs within human prostate cancer cells.[174]

Tomography can also be coupled with XAS in order to get a 3D chemical information. For instance, near-edge absorption soft X-ray nanotomography (NEASXT) was used to

determine the distribution of cubic SPIONs of around 14 nm within human adenocarcinoma cells, at a 50 nm resolution (**Figure 14D**).[175] Tilt-series were acquired at 700 eV and 709 eV, corresponding to the iron L_3 absorption edge, to specifically detect the absorption changes corresponding to SPIONs, as the absorption of cellular components was constant at these two energies.

Despite the high potential of X-ray approaches, the huge majority of studies undertake correlative investigations. For instance, cryo-SXT has been combined with Surface Enhanced Raman Scattering (SERS) spectroscopy to determine the NCs-cell interactions from their specific vibrational signature. With this approach, the uptake mechanism of silver NPs was monitored within fibroblasts and macrophages with a resolution of 36 nm.[176] While cryo-SXT demonstrated the formation of NP ring-shape structures inside endosomes, SERS revealed the relation with the specific interactions between the NPs surface and biomolecules surrounding them. Recently, Szekeres *et al.*[177] combined cryo-soft X-ray nanotomography, SERS and MS to monitor the formation of a protein corona around gold NPs (30 nm) when internalized within epithelial cells. It was demonstrated that the uptake mechanism and intracellular fate of the NPs depend on their protein corona composition.

This summary offers a quick insight of the X-rays spectromicroscopy techniques that can be employed to characterize NCs and assess their interactions with biological systems. Although non-exhaustive (other examples can be found in [178]), it reveals the high potential of these techniques which were limited by their poor spatial resolution for a long time but have recently undergone notable improvements. Noteworthy, the large majority of the present examples used a multimodal approach by combining X-ray and electron spectromicroscopies. Both are complementary: the first has high spectral resolution and sensitivity, and requires minimal sample preparation, while the last provides structural and chemical information with a higher spatial resolution.

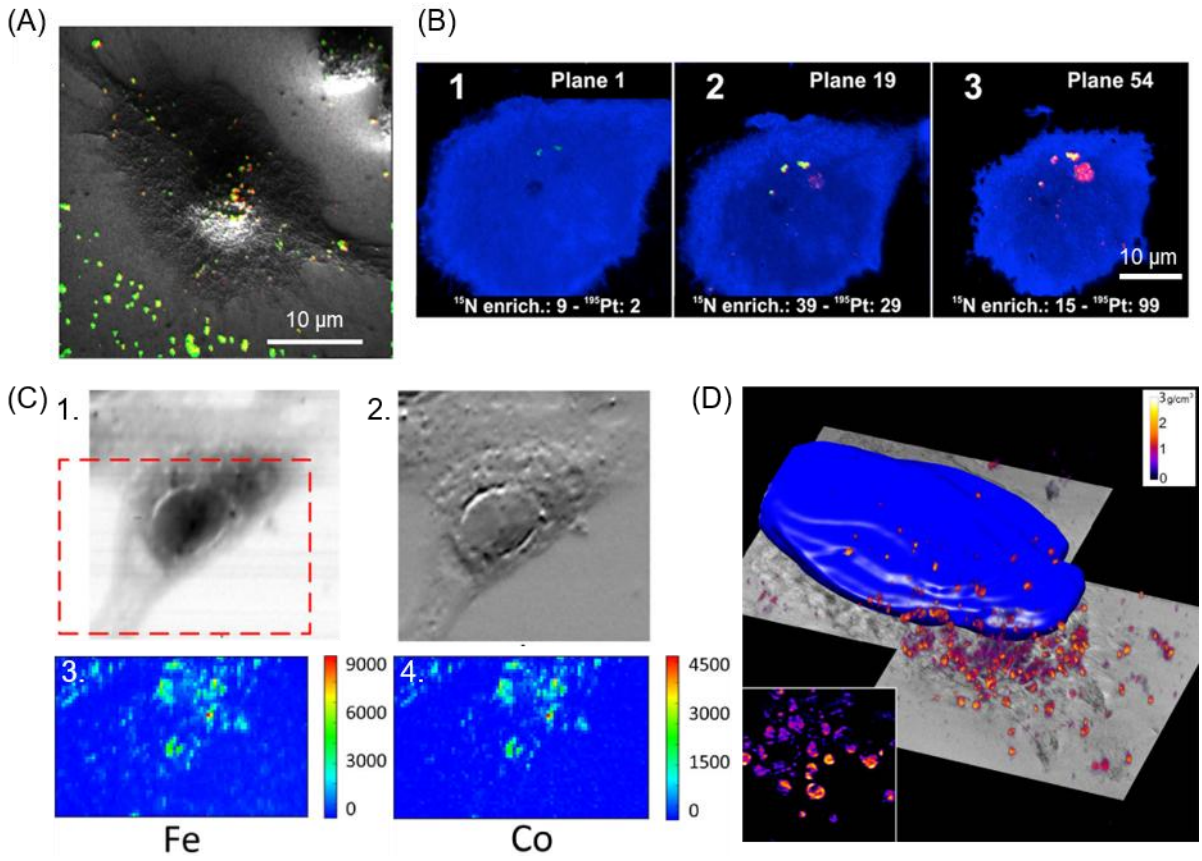

Figure 14: NanoSIMS and Synchrotron based-X-ray spectromicroscopies: NanoSIMS maps from Hela cells incubated with polymeric NPs labelled with ^{15}N and loaded with oxaliplatin from [139] . Red and green colors represent ^{195}Pt and ^{15}N signals while yellow color corresponds to the colocalization of those two signals: (A) ^{15}N and ^{195}Pt maps overlaid on the secondary electron image of the cell; (B) Successive maps from an HeLa cell incubated 24h with NPs obtained by removing layers of organic matter from the cell surface and subsequent imaging. The cell surface is represented by the $^{12}C^{14}N^-$ ion map (in blue). (C) Top images correspond to the absorption (1) and phase (2) contrast images of $CoFe_2O_4$ NPs internalized within a human glioblastoma-astrocytoma cell. The corresponding XRF maps of Fe (3) and Co (4) are presented (bottom images) for the region of interest indicated in red in (C1) (40 x 40 µm² size).[158] (D) 3D representation of SPION densities within human adenocarcinoma cells (color grading = 0-3 g/cm^3 from purple to white). Blue area represents the nucleus and red to yellow areas the SPION distribution.[175] (A-B) Adapted with permission.[139] Copyright 2016, American Chemical Society. (C) Adapted with permission.[158] Copyright 2013, Wiley Ltd. (D) Adapted under the terms and conditions of the Creative Commons Attribution 4.0 International License.[175] Copyright 2016, Springert Nature.

6. Perspectives

The analytical tools to characterize NCs on an individual basis attract a growing interest. It is more and more acknowledged that accurate measurements of size distributions should be based on tracking individual NPs. In the case of TRPS, engineered functionalized membranes are under development, whereas for NTA, data analysis methods are adjusted to take into account polydisperse samples.[179]

For many years, TEM has been the method of choice to investigate biological systems. The possibilities offered by cryo-TEM to study NC samples in 2D and 3D at HR in their hydrated environment have not been fully exploited so far. The recent introduction of direct electron detectors that enable HR imaging in cryo-conditions down to nearly atomic scales is revolutionary. Remarkably, this approach makes it possible to address the dynamic aspects of processes such as the conformational variation of flexible objects or their assembly pathways as done for DNA-nanogold conjugates[180] and hybrid albumin-MOFs.[181]

A very promising STEM approach is integrated differential phase contrast (iDPC) imaging that allows a better detection of light elements among heavy ones compared with conventional HAADF imaging.[182] Moreover, this technique has a signal-to-noise ratio better than other STEM modes such as ADF and HAADF. As a result, beam-sensitive specimens can be imaged, such as zeolite crystals,[67][183][184] with a sub-Å resolution at ultra-low electron doses (< 40 e^{-} $Å^{-2}$), 2-3 orders of magnitude lower than that used in conventional STEM.

Another major interest of STEM lies in the possibility to characterize the chemical species by EELS spectromicroscopy at very high spatial resolution, down to the atomic scale.[39][81][185] This is also true for XANES, but both techniques have rarely been exploited so far to distinguish between chemical species[186] despite that they can provide a complete identification of organic compounds.[187] This could give very valuable information for organic NC identification in biological environments, without need of labelling. Recent advances are pushing back the limits of these techniques. For instance, sub-10 nm resolutions are now achieved by cryo-soft X-ray ptychography.[188] For EELS, recent advances concerning STEM monochromators and EELS direct detectors have increased the energy resolution below 5 meV together with the sensitivity of the analysis.[189]

Concerning 3D-imaging, FIB-SEM is undeniably the method of choice to image very large volumes, up to 10^7 μm^3 with a high isotropic resolution (voxel sizes of 8 x 8 x 8 nm) compatible with the imaging of the smallest cellular organelles.[190] 3D-SEM can be applied to vitrified, hydrated and unstained specimens[191][192] Cryo-SXT constitutes a very promising approach for 3D investigations of NCs in relatively thick samples (~µm). No contrast enhancement is required to image samples, thus avoiding chemical treatments[193].

Improvements in near-field microscopies have also enabled to characterize NPs in their native state. Although AFM has the advantage to allow operating within fluid cells it is difficult to achieve a good fixation of NCs on their support during investigations in liquid state and cantilever oscillations are prone to be dampened by water.[194] Thanks to technical advances, nanoscale resolved *in liquid* s-SNOM and PTIR have been demonstrated for catalase nanocrystals and biomimetic peptoid nanosheets,[195] organic monolayers[196][197] and bilayers,[198] single-wall carbon nanotubes,[199] functionalized gold triangles,[200] chemical reactions at the solid-liquid interface,[201][202] living cells,[203] thin poly(methyl methacrylate) films[204] and amyloid peptide fibrils.[205] Further perspectives are intended to extend the IR spectral range of the analysis to enlarge the NC detection possibilities in biological media but more investigations are needed to improve the relatively weak spatial resolution of this promising approach.[206]

Another important challenge in nanomedicine is the quantitative analysis of the NC components (drugs, shells, targeting ligands) on an individual NCs basis. This would be of main interest in terms of quality assessment of drug formulations, as the drug loading would be determined on an individual NC basis. Despite an attempt made on a poly-methyl-methacrylate films,[207] quantification by PTIR remains an arduous task. While the relatively recent PTIR technique is still in progress, it is a promising tool that increasingly attracts attention.

Although near-field optical microscopies are able to identify and characterize NCs and their interactions with biomaterials, their spatial resolution cannot compete with EM. Correlative studies as TEM/s-SNOM and TEM/PTIR are then crucial to overcome this limitation and deeply analyze the samples.[208]–[210] Even farther, complementary techniques can be integrated to the setup of a near-field optical microscopes such as ultrasonic holography[211]–[213] or confocal microscopy.[214] These interesting improvements can particularly be used to unambiguously identify the intracellular compartments where the NCs are located.

7. Conclusion

Nanomedicines gain increasing interest in the treatment of severe diseases such as cancer and infections. Multifunctional NCs with sizes usually lower than 200 nm possess complex core-shell structures, composed of synergic drugs and engineered coatings bearing targeting ligands. In the journey from bench to bedside, the comprehensive characterization of the NCs and the knowledge of their interaction with the living media, especially targeted cells, is fundamental but challenging. This review highlighted that the methods allowing to characterize the NCs on an individual basis are key in terms of quality control of NC formulations and to study their biological fate.

The NCs' size distribution is commonly determined by DLS, but this "bulk" technique gives average values and is sensitive to the population with largest sizes. In this context, other techniques (NTA, SPES and TRPS) were developed to measure size distribution and sometimes other properties such as surface charge, based on individual NC analysis. These techniques can be applied whatever the nature (organic, inorganic or hybrid) of the sample.

EM are the principal characterization tools to observe drug NCs and to investigate their interaction with biological systems. Seeing the unseen is the art of microscopy and the examples presented here highlight the usefulness of advanced EM techniques to decipher the structure and composition of individual drug NCs. Vital to scientists, microscopy allows to visualize and interrogate phenomena occurring beyond the reach of the naked eye, while capturing sometimes aesthetic patterns as shown in the images presented here. TEM investigations are limited to NCs below 500 nm compatible with the transmission of the electron beam through the specimen but thicker samples (cells, tissues with NCs) can be also analyzed after sectioning. Cryo-EM allow imaging of low contrast NCs as organic ones in conditions close to their native state, in aqueous media, with sub- nanometric spatial resolution..

Advantageously, for chemical mapping, EMs have been coupled to analytical tools based on spectroscopic analysis, providing information at the nanoscale about the chemical compositions, morphologies, sizes and cellular localizations of a large variety of NCs. However, these approaches are limited to the analysis of a reduced volume that may be not statistically representative of the complete specimen The combination and comparison with

bulk approaches giving information on the complete specimen allow to bypass these drawbacks.

Near-field microscopy approaches are of peculiar interest in the study of NCs. s-SNOM is well adapted for NCs which strongly scatter the light, such as metal NCs as small as 50 nm, but not well appropriated for poorly scattering samples such as organic NCs. NanoSIMS is also well adapted for metal NCs but the spatial resolution is lower, and investigation of organic samples needs labelling with isotopes. The first technique able to detect unlabelled polymeric NCs in cells was Raman microspectroscopy, offering the possibility to perform imaging together with chemical analysis. However, the resolution was limited by light diffraction to 300 nm - 1 µm and Raman signal is usually overwhelmed by the large cell autofluorescence. In contrast, PTIR enabled detecting unlabelled polymeric NCs as small as 150 nm inside the cells. Moreover, the distribution of the components of individual NCs was unambiguously determined. PTIR is gaining increasing interest for the polymeric soft NC investigation and has potential for quantitative analysis.

Important achievements were made by Synchrotron-based X-ray spectromicroscopy which emerged as a highly sensitive approach to map quantitatively sample chemical composition with sub-micron resolution. These characterizations were mostly applied on inorganic NCs.

In a nutshell, the methods used to investigate individual NCs allowed: i) studying the morphology and the crystalline structure of the NCs; ii) localizing the components of an individual NC (drugs, coatings, ligands); iii) quantify the constituents in a NCs; iv) detecting NCs in cells and biological samples and v) exploring the fate (degradation, drug release) of a NC in a biological media.

However, all nanoscale approaches are subject to potential artefacts and are limited to the analysis of NCs with a specific size range, chemical nature and morphology. The investigation tools need to be carefully chosen according to the question(s) to be addressed and statistically relevant analyses have to be performed. There is no universal method allowing a full NC characterization and combinatorial approaches are essential. Whereas~~,~~ the individual NC characterization approaches are expected to gain increasing interest in the near future, their combination with “bulk” approaches is essential to gain in depth information of NCs.

List of abbreviations

2D	Two-dimension
3D	Three-dimension
ADF	Annular Dark-Field
AFM	Atomic Force Microscopy
AFM-IR	Atomic Force Microscopy-based Infrared
BF	Bright Field
CNT	Carbon Nanotube
Cryo-SXT	Cryo-Soft X-ray Tomography
CTEM	Conventional Transmission Electron Microscopy
DCS	Differential Centrifugal Sedimentation
DF	Dark-field
DLS	Dynamic Light Scattering
EDX, EDXS, EDS	Energy dispersive X-ray spectroscopy,
EELS	Electron Energy Loss Spectroscopy,
EFTEM	Energy Filter Transmission Electron Microscopy
ELS	Electrophoretic Light Scattering
EM	Electron microscopy
ET	Electron tomography
FDA	Food and Drug Administration
FEG	Field Emission Gun
FFF	Field Flow Fractionation
FIB	Focused Ion Beam
FTIR	Fourier Transform Infrared
HAADF	High-Angle Annular Dark-Field
HPLC	High Performance Liquid Chromatography
HRTEM	High-resolution Transmission Electron Microscopy
MALDI	Matrix Assisted Laser Desorption Ionisation
MIL	Material of Institute Lavoisier
MOF	Metal-Organic Framework
MSN	Mesoporous Silica Nanoparticle

Nano-FTIR spectroscopy	Fourier Transform Infrared Nanospectroscopy
NC	Nanocarrier
NEASXT	Near-Edge Absorption Soft X-ray Nanotomography
NEXAFS	Near Edge X-ray Absorption near edge Fine structure
NMR	Nuclear Magnetic Resonance
NP	Nanoparticle
NTA	Nanoparticle Tracking Analysis
PAA	Poly(acrylic acid)
PEG	Poly(ethylene glycol)
PIP	Pipemidic acid
PLA	Poly(lactic acid)
PLGA	Poly(lactic-co-glycolic acid)
PS	Polystyrene
PTIR	Photothermal Induced Resonances
SAXS	Small Angle X-rays Scattering
SBF-SEM	Serial Block-Face Scanning Electron Microscopy
SEM	Scanning Electron Microscopy
SERS	Surface Enhanced Raman Scattering
SIMS	Secondary Ion Mass Spectroscopy
SPA	Single Particle Analysis
SPES	Single Particle Extinction and Scattering
SPION	Superparamagnetic Iron Oxide Nanoparticle
s-SNOM	Scattering-type Scanning Near-Field Optical Microscopy
STEM	Scanning Transmission Electron Microscopy
STM	Scanning Tunnelling Microscopy
STXM	Scanning Transmission X-ray Microscopy
TEM	Transmission Electron Microscopy
TERS	Tip-Enhanced Raman Scattering
TGA	Thermogravimetric Analysis
ToF-SIMS	Time-of-flight secondary ion mass spectrometry
TRPS	Tunable Resistive Pulse Sensing

TXM	Transmission X-ray Microscopy
UiO	Universitetet i Oslo
UV-Vis	Ultraviolet-visible Spectrophotometry
XANES	X-ray Absorption Near-Edge Structure
XAS	X-ray Absorption Spectroscopy
XPS	X-ray Photoelectron Spectroscopy
XRD	X-Ray Diffraction
XRF	X-Ray Fluorescence spectroscopy

References

[1] Z. Zhao, A. Ukidve, V. Krishnan, S. Mitragotri, *Adv. Drug Deliv. Rev.* **2019**, *143*, 3.
[2] J.B. Finean, M.G. Rumsby, *Nature* **1963**, *200*, 1340.
[3] D.J.A. Crommelin, P. van Hoogevest, G. Storm, *J. Controlled Release* **2020**, *318*, 256.
[4] A.C. Anselmo, S. Mitragotri, *Bioeng. Transl. Med.* **2019**, *4*, e10143.
[5] A.-A.D. Jones, G. Mi, T.J. Webster, *Trends Biotechnol.* **2019**, *37*, 117.
[6] *Nat. Nanotechnol.* **2020**, *15*, 963.
[7] E. Sánchez-López, D. Gomes, G. Esteruelas, L. Bonilla, A.L. Lopez-Machado, R. Galindo, A. Cano, M. Espina, M. Ettcheto, A. Camins, A.M. Silva, A. Durazzo, A. Santini, M.L. Garcia, E.B. Souto, *Nanomaterials* **2020**, *10*, 292.
[8] X. Li, E. Porcel, M. Menendez-Miranda, J. Qiu, X. Yang, C. Serre, A. Pastor, D. Desmaële, S. Lacombe, R. Gref, *ChemMedChem* **2020**, *15*, 274.
[9] H. Sharma, P.K. Mishra, S. Talegaonkar, B. Vaidya, *Drug Discov. Today* **2015**, *20*, 1143.
[10] P. Horcajada, T. Chalati, C. Serre, B. Gillet, C. Sebrie, T. Baati, J.F. Eubank, D. Heurtaux, P. Clayette, C. Kreuz, J.-S. Chang, Y.K. Hwang, V. Marsaud, P.-N. Bories, L. Cynober, S. Gil, G. Férey, P. Couvreur, R. Gref, *Nat. Mater.* **2010**, *9*, 172.
[11] A. Ahmad, F. Khan, R.K. Mishra, R. Khan, *J. Med. Chem.* **2019**, *62*, 10475.
[12] R. Gref, A. Domb, P. Quellec, T. Blunk, R.H. Müller, J.M. Verbavatz, R. Langer, *Adv. Drug Deliv. Rev.* **2012**, *64*, 316.
[13] O. Harush-Frenkel, E. Rozentur, S. Benita, Y. Altschuler, *Biomacromolecules* **2008**, *9*, 435.
[14] J.J. Rennick, A.P.R. Johnston, R.G. Parton, *Nat. Nanotechnol.* **2021**, *16*, 266.
[15] R.A. Petros, J.M. DeSimone, *Nat. Rev. Drug Discov.* **2010**, *9*, 615.
[16] E. Hinde, K. Thammasiraphop, H.T.T. Duong, J. Yeow, B. Karagoz, C. Boyer, J.J. Gooding, K. Gaus, *Nat. Nanotechnol.* **2017**, *12*, 81.
[17] J. Panyam, V. Labhasetwar, *Adv. Drug Deliv. Rev.* **2003**, *55*, 329.
[18] S.K. Sahoo, J. Panyam, S. Prabha, V. Labhasetwar, *J. Controlled Release* **2002**, *82*, 105.
[19] S.M. Stavis, J.A. Fagan, M. Stopa, J.A. Liddle, *ACS Appl. Nano Mater.* **2018**, *1*, 4358.
[20] J.-M. Rabanel, V. Adibnia, S. F. Tehrani, S. Sanche, P. Hildgen, X. Banquy, C. Ramassamy, *Nanoscale* **2019**, *11*, 383.
[21] T.L. Andresen, J.B. Larsen, *Acta Biomater.* **2020**, *118*, 207.
[22] D. Duchêne, R. Gref, *Int. J. Pharm.* **2016**, *502*, 219.
[23] V. Klang, C. Valenta, N.B. Matsko, *Micron* **2013**, *44*, 45.
[24] J. Kuntsche, J.C. Horst, H. Bunjes, *Int. J. Pharm.* **2011**, *417*, 120.
[25] E. Manaia, B. Chiari-Andréo, B. Silva, J. Oshiro Junior, L. Chiavacci, *Int J Nanomedicine* **2017**, *12*, 4991.
[26] A. Brown, N. Hondow, in *Front. Nanosci.* (Ed: H. Summers), Elsevier**2013**, 95.
[27] M. Reifarth, S. Hoeppener, U.S. Schubert, *Adv. Mater.* **2018**, *30*, 1703704.
[28] S. Wang, C.M. McGuirk, M.B. Ross, S. Wang, P. Chen, H. Xing, Y. Liu, C.A. Mirkin, *J. Am. Chem. Soc.* **2017**, *139*, 9827.
[29] D. Niu, Z. Liu, Y. Li, X. Luo, J. Zhang, J. Gong, J. Shi, *Adv. Mater.* **2014**, *26*, 4947.
[30] K.A. Eid, H.M. Azzazy, *Int. J. Nanomedicine* **2012**, *7*, 1543.
[31] N. Ž. Knežević, J.-O. Durand, *Nanoscale* **2015**, *7*, 2199.
[32] Q. He, J. Shi, F. Chen, M. Zhu, L. Zhang, *Biomaterials* **2010**, *31*, 3335.
[33] H. Li, H. Yu, C. Zhu, J. Hu, M. Du, F. Zhang, D. Yang, *RSC Adv.* **2016**, *6*, 94160.
[34] J.R. Morones, J.L. Elechiguerra, A. Camacho, K. Holt, J.B. Kouri, J.T. Ramírez, M.J. Yacaman, *Nanotechnology* **2005**, *16*, 2346.
[35] N.Q. Yin, P. Wu, T.H. Yang, M. Wang, *RSC Adv.* **2017**, *7*, 9123.
[36] J. Hitchcock, A.L. White, N. Hondow, T.A. Hughes, H. Dupont, S. Biggs, O.J. Cayre, *J. Colloid Interface Sci.* **2020**, *567*, 171.
[37] R. Mahugo, A. Mayoral, M. Sánchez-Sánchez, I. Diaz, *Front. Chem.* **2019**, *7*.

[38] A. Fondell, K. Edwards, L.M. Ickenstein, S. Sjöberg, J. Carlsson, L. Gedda, *Eur. J. Nucl. Med. Mol. Imaging* **2009**, *37*, 114.
[39] A. Gloter, V. Badjeck, L. Bocher, N. Brun, K. March, M. Marinova, M. Tencé, M. Walls, A. Zobelli, O. Stéphan, C. Colliex, *Mater. Sci. Semicond. Process.* **2017**, *65*, 2.
[40] L.L. Félix, B. Sanz, V. Sebastián, T.E. Torres, M.H. Sousa, J. a. H. Coaquira, M.R. Ibarra, G.F. Goya, *Sci. Rep.* **2019**, *9*, 1.
[41] P. Brüggeller, E. Mayer, *Nature* **1980**, *288*, 569.
[42] J. Dubochet, A.W. McDowall, *J. Microsc.* **1981**, *124*, 3.
[43] D. Danino, *Curr. Opin. Colloid Interface Sci.* **2012**, *17*, 316.
[44] H. Friedrich, P.M. Frederik, G. de With, N.A.J.M. Sommerdijk, *Angew. Chem. Int. Ed.* **2010**, *49*, 7850.
[45] V. Lučić, A. Rigort, W. Baumeister, *J. Cell Biol.* **2013**, *202*, 407.
[46] R.F. Thompson, M. Walker, C.A. Siebert, S.P. Muench, N.A. Ranson, *Methods* **2016**, *100*, 3.
[47] L.M. Ickenstein, M.C. Sandström, L.D. Mayer, K. Edwards, *Biochim. Biophys. Acta BBA - Biomembr.* **2006**, *1758*, 171.
[48] J. Barauskas, A. Misiunas, T. Gunnarsson, F. Tiberg, M. Johnsson, *Langmuir* **2006**, *22*, 6328.
[49] J.W. Wills, H.D. Summers, N. Hondow, A. Sooresh, K.E. Meissner, P.A. White, P. Rees, A. Brown, S.H. Doak, *ACS Nano* **2017**, *11*, 11986.
[50] R.I. Koning, A.J. Koster, T.H. Sharp, *Ann. Anat. - Anat. Anz.* **2018**, *217*, 82.
[51] Y. Cheng, *Cell* **2015**, *161*, 450.
[52] R. Fernandez-Leiro, S.H.W. Scheres, *Nature* **2016**, *537*, 339.
[53] K.R. Vinothkumar, R. Henderson, *Q. Rev. Biophys.* **2016**, *49*.
[54] K. Murata, M. Wolf, *Biochim. Biophys. Acta BBA - Gen. Subj.* **2018**, *1862*, 324.
[55] P.L. Stewart, *WIREs Nanomedicine Nanobiotechnology* **2017**, *9*, e1417.
[56] S. Guo, M. Vieweger, K. Zhang, H. Yin, H. Wang, X. Li, S. Li, S. Hu, A. Sparreboom, B.M. Evers, Y. Dong, W. Chiu, P. Guo, *Nat. Commun.* **2020**, *11*, 1.
[57] H. Azhari, M. Strauss, S. Hook, B.J. Boyd, S.B. Rizwan, *Eur. J. Pharm. Biopharm.* **2016**, *104*, 148.
[58] J.S. Lengyel, J.L. Milne, S. Subramaniam, *Nanomed.* **2008**, *3*, 125.
[59] C. Bonnaud, C.A. Monnier, D. Demurtas, C. Jud, D. Vanhecke, X. Montet, R. Hovius, M. Lattuada, B. Rothen-Rutishauser, A. Petri-Fink, *ACS Nano* **2014**, *8*, 3451.
[60] O. Le Bihan, P. Bonnafous, L. Marak, T. Bickel, S. Trépout, S. Mornet, F. De Haas, H. Talbot, J.-C. Taveau, O. Lambert, *J. Struct. Biol.* **2009**, *168*, 419.
[61] P. Ercius, O. Alaidi, M.J. Rames, G. Ren, *Adv. Mater.* **2015**, *27*, 5638.
[62] A. Balfourier, N. Luciani, G. Wang, G. Lelong, O. Ersen, A. Khelfa, D. Alloyeau, F. Gazeau, F. Carn, *Proc. Natl. Acad. Sci.* **2020**, *117*, 103.
[63] A. Guven, I.A. Rusakova, M.T. Lewis, L.J. Wilson, *Biomaterials* **2012**, *33*, 1455.
[64] C. Hoskins, Y. Min, M. Gueorguieva, C. McDougall, A. Volovick, P. Prentice, Z. Wang, A. Melzer, A. Cuschieri, L. Wang, *J. Nanobiotechnology* **2012**, *10*, 27.
[65] R. Leapman, in *Transm. Electron Energy Loss Spectrom. Mater. Sci. EELS Atlas*, John Wiley & Sons, Ltd**2005**, 49.
[66] S. Ristig, O. Prymak, K. Loza, M. Gocyla, W. Meyer-Zaika, M. Heggen, D. Raabe, M. Epple, *J. Mater. Chem. B* **2015**, *3*, 4654.
[67] B. Shen, X. Chen, D. Cai, H. Xiong, X. Liu, C. Meng, Y. Han, F. Wei, *Adv. Mater.* **2019**, *32*, 1906103.
[68] L.H. Bryant, S.J. Kim, M. Hobson, B. Milo, Z.I. Kovacs, N. Jikaria, B.K. Lewis, M.A. Aronova, A.A. Sousa, G. Zhang, R.D. Leapman, J.A. Frank, *Nanomedicine Nanotechnol. Biol. Med.* **2017**, *13*, 503.
[69] A.-V. Weiss, M. Koch, M. Schneider, *Int. J. Pharm.* **2019**, *570*, 118650.
[70] Z. Shen, J. Song, Z. Zhou, B.C. Yung, M.A. Aronova, Y. Li, Y. Dai, W. Fan, Y. Liu, Z. Li, H. Ruan, R.D. Leapman, L. Lin, G. Niu, X. Chen, A. Wu, *Adv. Mater.* **2018**, *30*, 1803163.
[71] A.M. Schrand, J.J. Schlager, L. Dai, S.M. Hussain, *Nat. Protoc.* **2010**, *5*, 744.

[72] R. Di Corato, A. Espinosa, L. Lartigue, M. Tharaud, S. Chat, T. Pellegrino, C. Ménager, F. Gazeau, C. Wilhelm, *Biomaterials* **2014**, *35*, 6400.
[73] C. He, K. Lu, W. Lin, *J. Am. Chem. Soc.* **2014**, *136*, 12253.
[74] X. Li, N. Semiramoth, S. Hall, V. Tafani, J. Josse, F. Laurent, G. Salzano, D. Foulkes, P. Brodin, L. Majlessi, N.-E. Ghermani, G. Maurin, P. Couvreur, C. Serre, M.-F. Bernet-Camard, J. Zhang, R. Gref, *Part. Part. Syst. Charact.* **2019**, *36*, 1800360.
[75] K.L. Mcdonald, *J. Microsc.* **2009**, *235*, 273.
[76] D. Hofmann, S. Tenzer, M.B. Bannwarth, C. Messerschmidt, S.-F. Glaser, H. Schild, K. Landfester, V. Mailänder, *ACS Nano* **2014**, *8*, 10077.
[77] A.-K. Barthel, M. Dass, M. Dröge, J.-M. Cramer, D. Baumann, M. Urban, K. Landfester, V. Mailänder, I. Lieberwirth, *Beilstein J. Nanotechnol.* **2014**, *5*, 1905.
[78] R. Kalluru, F. Fenaroli, D. Westmoreland, L. Ulanova, A. Maleki, N. Roos, M.P. Madsen, G. Koster, W. Egge-Jacobsen, S. Wilson, H. Roberg-Larsen, G.K. Khuller, A. Singh, B. Nyström, G. Griffiths, *J. Cell Sci.* **2013**, *126*, 3043.
[79] N. Singh, G.J.S. Jenkins, B.C. Nelson, B.J. Marquis, T.G.G. Maffeis, A.P. Brown, P.M. Williams, C.J. Wright, S.H. Doak, *Biomaterials* **2012**, *33*, 163.
[80] E. Allard-Vannier, K. Hervé-Aubert, K. Kaaki, T. Blondy, A. Shebanova, K.V. Shaitan, A.A. Ignatova, M.-L. Saboungi, A.V. Feofanov, I. Chourpa, *Biochim. Biophys. Acta BBA - Gen. Subj.* **2017**, *1861*, 1578.
[81] C. Gay, E. Letavernier, M.-C. Verpont, M. Walls, D. Bazin, M. Daudon, N. Nassif, O. Stéphan, M. de Frutos, *ACS Nano* **2020**, *14*, 1823.
[82] I. Cabezón, E. Augé, M. Bosch, A.J. Beckett, I.A. Prior, C. Pelegrí, J. Vilaplana, *Histochem. Cell Biol.* **2017**, *148*, 3.
[83] V. Mollo, P. Scognamiglio, A. Marino, G. Ciofani, F. Santoro, *Adv. Mater. Technol.* **2020**, *5*, 1900687.
[84] P.K. Hansma, J. Tersoff, *J. Appl. Phys.* **1987**, *61*, R1.
[85] A. Rodríguez-Galván, O. Amelines-Sarria, M. Rivera, M. del P. Carreón-Castro, V.A. Basiuk, *Nano* **2016**.
[86] S. Sadaf, L. Walder, *Adv. Mater. Interfaces* **2017**, *4*.
[87] D.A. Yarotski, S.V. Kilina, A.A. Talin, S. Tretiak, O.V. Prezhdo, A.V. Balatsky, A.J. Taylor, *Nano Lett.* **2009**, *9*, 12.
[88] C.J. Fleming, Y.X. Liu, Z. Deng, G. Liu, *J. Phys. Chem. A* **2009**, *113*, 4168.
[89] C.J. Fleming, N.-N. Yin, S.L. Riechers, G. Chu, G. Liu, *ACS Nano* **2011**, *5*, 1685.
[90] S. Riechers, Q. Zhong, N.-N. Yin, A. Karsai, S.R.P. da Rocha, G. Liu, *J. Drug Deliv.* **2015**, *2015*.
[91] L. Shi, C.J. Fleming, S.L. Riechers, N.-N. Yin, J. Luo, K.S. Lam, G. Liu, *J. Drug Deliv.* **2011**, *2011*.
[92] P. Eaton, P. West, *Atomic Force Microscopy*, Oxford University Press, Oxford, New York **2010**.
[93] R. Gref, Y. Minamitake, M.T. Peracchia, V. Trubetskoy, V. Torchilin, R. Langer, *Science* **1994**, *263*, 1600.
[94] J.R. Smith, T.O.B. Olusanya, D.A. Lamprou, *Expert Opin. Drug Deliv.* **2018**, *15*, 1211.
[95] Y. M. Efremov, T. Okajima, A. Raman, *Soft Matter* **2020**, *16*, 64.
[96] A. zur Mühlen, E. zur Mühlen, H. Niehus, W. Mehnert, *Pharm. Res.* **1996**, *13*, 1411.
[97] D.A. Lamprou, V. Venkatpurwar, M.N.V.R. Kumar, *PLOS ONE* **2013**, *8*, e64490.
[98] Y.F. Dufrêne, T. Ando, R. Garcia, D. Alsteens, D. Martinez-Martin, A. Engel, C. Gerber, D.J. Müller, *Nat. Nanotechnol.* **2017**, *12*, 295.
[99] L. Urbina, A. Eceiza, N. Gabilondo, M.Á. Corcuera, A. Retegi, *Int. J. Biol. Macromol.* **2020**, *163*, 1249.
[100] H. Lee, Y. Hong, D. Lee, S. Hwang, G. Lee, J. Yang, D.S. Yoon, *Nanotechnology* **2020**, *31*, 215706.
[101] A. Rodzinski, R. Guduru, P. Liang, A. Hadjikhani, T. Stewart, E. Stimphil, C. Runowicz, R. Cote, N. Altman, R. Datar, S. Khizroev, *Sci. Rep.* **2016**, *6*, 20867.
[102] C. Dong, S. Corsetti, D. Passeri, M. Rossi, M. Carafa, F. Pantanella, F. Rinaldi, C. Ingallina, A. Sorbo, C. Marianecci, *AIP Conf. Proc.* **2015**, *1667*, 020011.

[103] D. Passeri, C. Dong, M. Reggente, L. Angeloni, M. Barteri, F.A. Scaramuzzo, F.D. Angelis, F. Marinelli, F. Antonelli, F. Rinaldi, C. Marianecci, M. Carafa, A. Sorbo, D. Sordi, I.W. Arends, M. Rossi, *Biomatter* **2014**, *4*, e29507.
[104] H. Shen, D. Long, L. Zhu, X.-Y. Li, Y. Dong, N. Jia, H. Zhou, X. Xin, Y. Sun, *Biophys. Chem.* **2006**, *122*, 1.
[105] Z. Wang, A. Cuschieri, *Int. J. Mol. Sci.* **2013**, *14*, 9111.
[106] Y. Zhang, M. Yang, M. Ozkan, C.S. Ozkan, *Biotechnol. Prog.* **2009**, *25*, 923.
[107] G. Pyrgiotakis, C.O. Blattmann, P. Demokritou, *ACS Sustain. Chem. Eng.* **2014**, *2*, 1681.
[108] Y. Dror, R. Sorkin, G. Brand, O. Boubriak, J. Urban, J. Klein, *Sci. Rep.* **2017**, *7*, 45758.
[109] A. Centrone, *Annu. Rev. Anal. Chem.* **2015**, *8*, 101.
[110] X. Chen, D. Hu, R. Mescall, G. You, D.N. Basov, Q. Dai, M. Liu, *Adv. Mater.* **2019**, *31*, 1804774.
[111] Z. Nuño, B. Hessler, J. Ochoa, Y.-S. Shon, C. Bonney, Y. Abate, *Opt. Express* **2011**, *19*, 20865.
[112] R.J. Hermann, M.J. Gordon, *Annu. Rev. Chem. Biomol. Eng.* **2018**, *9*, 365.
[113] D. Kurouski, A. Dazzi, R. Zenobi, A. Centrone, *Chem. Soc. Rev.* **2020**, *49*, 3315.
[114] M. Ashtikar, L. Langelüddecke, A. Fahr, V. Deckert, *Biochim. Biophys. Acta BBA - Gen. Subj.* **2017**, *1861*, 2630.
[115] I. Amenabar, S. Poly, M. Goikoetxea, W. Nuansing, P. Lasch, R. Hillenbrand, *Nat. Commun.* **2017**, *8*, 14402.
[116] L.B. Capeletti, J.F.A. de Oliveira, L.M.D. Loiola, F.E. Galdino, D.E. da S. Santos, T.A. Soares, R. de O. Freitas, M.B. Cardoso, *Adv. Funct. Mater.* **2019**, *29*, 1904216.
[117] A. Dazzi, R. Prazeres, F. Glotin, J.M. Ortega, *Opt. Lett.* **2005**, *30*, 2388.
[118] H. Zhou, Y. Tang, S. Zhang, in *Smart Nanocontainers* (Eds: P. Nguyen-Tri, T.-O. Do, T.A. Nguyen), Elsevier**2020**, 7.
[119] J. Mathurin, E. Pancani, A. Deniset-Besseau, K. Kjoller, C.B. Prater, R. Gref, A. Dazzi, *The Analyst* **2018**, *143*, 5940.
[120] K. Wieland, G. Ramer, V.U. Weiss, G. Allmaier, B. Lendl, A. Centrone, *Nano Res.* **2019**, *12*, 197.
[121] D. Khanal, I. Khatib, J. Ruan, D. Cipolla, F. Dayton, J.D. Blanchard, H.-K. Chan, W. Chrzanowski, *Anal. Chem.* **2020**, *92*, 9922.
[122] N. Piergies, E. Pięta, C. Paluszkiewicz, H. Domin, W.M. Kwiatek, *Nano Res.* **2018**, *11*, 4401.
[123] E. Pięta, C. Paluszkiewicz, W.M. Kwiatek, *Phys. Chem. Chem. Phys.* **2018**, *20*, 27992.
[124] N. Piergies, A. Dazzi, A. Deniset-Besseau, J. Mathurin, M. Oćwieja, C. Paluszkiewicz, W.M. Kwiatek, *Nano Res.* **2020**, *13*, 1020.
[125] N. Piergies, M. Oćwieja, C. Paluszkiewicz, W.M. Kwiatek, *Appl. Surf. Sci.* **2021**, *537*, 147897.
[126] E. Pięta, C. Petibois, C. Paluszkiewicz, W.M. Kwiatek, *Appl. Surf. Sci.* **2020**, *499*, 143975.
[127] E. Pancani, J. Mathurin, S. Bilent, M.-F. Bernet-Camard, A. Dazzi, A. Deniset-Besseau, R. Gref, *Part. Part. Syst. Charact.* **2018**, *35*, 1700457.
[128] K. Kemel, A. Deniset-Besseau, A. Baillet-Guffroy, V. Faivre, A. Dazzi, C. Laugel, *Int. J. Pharm.* **2020**, *579*, 119193.
[129] J. Stetefeld, S.A. McKenna, T.R. Patel, *Biophys. Rev.* **2016**, *8*, 409.
[130] B. Carr, M. Wright, *Innov. Pharm. Technol.* **2008**, *26*, 38.
[131] F. Varenne, A. Makky, M. Gaucher-Delmas, F. Violleau, C. Vauthier, *Pharm. Res.* **2016**, *33*, 1220.
[132] V. Filipe, A. Hawe, W. Jiskoot, *Pharm. Res.* **2010**, *27*, 796.
[133] M. a. C. Potenza, T. Sanvito, S. Argentiere, C. Cella, B. Paroli, C. Lenardi, P. Milani, *Sci. Rep.* **2015**, *5*, 18228.
[134] T. Sanvito, P. Bigini, M.V. Cavanna, F. Fiordaliso, M.B. Violatto, L. Talamini, M. Salmona, P. Milani, M.A.C. Potenza, *Nanomedicine Nanotechnol. Biol. Med.* **2017**, *13*, 2597.
[135] M.A. C. Potenza, Ž. Krpetić, T. Sanvito, Q. Cai, M. Monopoli, J.M. de Araújo, C. Cella, L. Boselli, V. Castagnola, P. Milani, K. A. Dawson, *Nanoscale* **2017**, *9*, 2778.
[136] Y. Pei, R. Vogel, C. Minelli, in *Charact. Nanoparticles* (Eds: V.-D. Hodoroaba, W.E.S. Unger, A.G. Shard), Elsevier**2020**, 117.
[137] A. Sikora, A.G. Shard, C. Minelli, *Langmuir* **2016**, *32*, 2216.

[138] C. Colliex, *Comptes Rendus Phys.* **2019**, *20*, 746.
[139] M.T. Proetto, C.R. Anderton, D. Hu, C.J. Szymanski, Z. Zhu, J.P. Patterson, J.K. Kammeyer, L.G. Nilewski, A.M. Rush, N.C. Bell, J.E. Evans, G. Orr, S.B. Howell, N.C. Gianneschi, *ACS Nano* **2016**, *10*, 4046.
[140] I. Lozić, R.V. Hartz, C.A. Bartlett, J.A. Shaw, M. Archer, P.S.R. Naidu, N.M. Smith, S.A. Dunlop, K.S. Iyer, M.R. Kilburn, M. Fitzgerald, *Biomaterials* **2016**, *74*, 200.
[141] P.J. Kempen, C. Hitzman, L.S. Sasportas, S.S. Gambhir, R. Sinclair, *MRS Online Proc. Libr. OPL* **2013**, *1569*, 157.
[142] J. Neunzehn, F. Draude, U. Golla-Schindler, H.F. Arlinghaus, H.-P. Wiesmann, *Surf. Interface Anal.* **2013**, *45*, 1340.
[143] A.V. Singh, H. Jungnickel, L. Leibrock, J. Tentschert, P. Reichardt, A. Katz, P. Laux, A. Luch, *Sci. Rep.* **2020**, *10*, 261.
[144] T. Paunesku, S. Vogt, B. Lai, J. Maser, N. Stojićević, K.T. Thurn, C. Osipo, H. Liu, D. Legnini, Z. Wang, C. Lee, G.E. Woloschak, *Nano Lett.* **2007**, *7*, 596.
[145] T. Liu, I. Kempson, M. de Jonge, D.L. Howard, B. Thierry, *Nanoscale* **2014**, *6*, 9774.
[146] L. Pascolo, B. Bortot, N. Benseny-Cases, A. Gianoncelli, G. Tosi, B. Ruozi, C. Rizzardi, E. De Martino, M.A. Vandelli, G.M. Severini, *Int. J. Nanomedicine* **2014**, *9*, 2791.
[147] M.W. Westneat, J.J. Socha, W.-K. Lee, *Annu. Rev. Physiol.* **2008**, *70*, 119.
[148] B. Luan, T. Friedrich, J. Zhai, V.A. Streltsov, B.W. Lindsey, J. Kaslin, M.D. de Jonge, J. Zhu, T.C. Hughes, X. Hao, *RSC Adv.* **2016**, *6*, 23550.
[149] H.A. Castillo-Michel, C. Larue, A.E. Pradas del Real, M. Cotte, G. Sarret, *Plant Physiol. Biochem.* **2017**, *110*, 13.
[150] A.P. Hitchcock, *J. Electron Spectrosc. Relat. Phenom.* **2015**, *200*, 49.
[151] M. Holt, R. Harder, R. Winarski, V. Rose, *Annu. Rev. Mater. Res.* **2013**, *43*, 183.
[152] C.M. Graf, M.C. Meinke, Q. Gao, S. Hadam, J. Raabe, W.S. M.d, U. Blume-Peytavi, J.M. Lademann, E. Ruhl, A. Vogt, *J. Biomed. Opt.* **2009**, *14*, 021015.
[153] C. Graf, D. Nordmeyer, S. Ahlberg, J. Raabe, A. Vogt, J. Lademann, F. Rancan, E. Rühl, in *Colloidal Nanoparticles Biomed. Appl. X*, International Society For Optics And Photonics**2015**, 93381L.
[154] A. Gianoncelli, R. Delfino, S. Sala, G. Kourousias, S. Giordani, F. Romano, G. Ricci, L. Pascolo, *Nucl. Instrum. Methods Phys. Res. Sect. B Beam Interact. Mater. At.* **2020**, *465*, 79.
[155] F. Cammisuli, S. Giordani, A. Gianoncelli, C. Rizzardi, L. Radillo, M. Zweyer, T. Da Ros, M. Salomé, M. Melato, L. Pascolo, *Sci. Rep.* **2018**, *8*, 706.
[156] A. Gianoncelli, F. Cammisuli, M. Altissimo, M. Salomé, O. Radillo, G. Ricci, S. Giordani, C. Rizzardi, L. Pascolo, *X-Ray Spectrom.* **2019**, *48*, 413.
[157] P. Marmorato, G. Ceccone, A. Gianoncelli, L. Pascolo, J. Ponti, F. Rossi, M. Salomé, B. Kaulich, M. Kiskinova, *Toxicol. Lett.* **2011**, *207*, 128.
[158] A. Gianoncelli, P. Marmorato, J. Ponti, L. Pascolo, B. Kaulich, C. Uboldi, F. Rossi, D. Makovec, M. Kiskinova, G. Ceccone, *X-Ray Spectrom.* **2013**, *42*, 316.
[159] A. Procopio, C. Cappadone, N. Zaccheroni, E. Malucelli, L. Merolle, A. Gianoncelli, A. Sargenti, G. Farruggia, F. Palomba, E. Rampazzo, S. Rapino, L. Prodi, S. Iotti, *Talanta* **2019**, *202*, 251.
[160] D. Kwon, H.W. Nho, T.H. Yoon, *J. Nanosci. Nanotechnol.* **2015**, *15*, 4229.
[161] D. Kwon, H.W. Nho, T.H. Yoon, *Colloids Surf. B Biointerfaces* **2014**, *122*, 384.
[162] K. Yamamoto, A. Klossek, R. Flesch, T. Ohigashi, E. Fleige, F. Rancan, J. Frombach, A. Vogt, U. Blume-Peytavi, P. Schrade, S. Bachmann, R. Haag, S. Hedtrich, M. Schäfer-Korting, N. Kosugi, E. Rühl, *J. Controlled Release* **2016**, *242*, 64.
[163] S. Matsuyama, K. Maeshima, M. Shimura, *J. Anal. At. Spectrom.* **2020**, *35*, 1279.
[164] B.D. Samber, E. Meul, B. Laforce, B.D. Paepe, J. Smet, M.D. Bruyne, R.D. Rycke, S. Bohic, P. Cloetens, R.V. Coster, P. Vandenabeele, T.V. Berghe, *PLOS ONE* **2018**, *13*, e0190495.
[165] K. Stachnik, M. Warmer, I. Mohacsi, V. Hennicke, P. Fischer, J. Meyer, T. Spitzbart, M. Barthelmess, J. Eich, C. David, C. Feldmann, B. Busse, K. Jähn, U.E. Schaible, A. Meents, *Sci. Rep.* **2020**, *10*, 1784.

[166] S. Yao, J. Fan, Z. Chen, Y. Zong, J. Zhang, Z. Sun, L. Zhang, R. Tai, Z. Liu, C. Chen, H. Jiang, *IUCrJ* **2018**, *5*, 141.
[167] M. Gallagher-Jones, C.S.B. Dias, A. Pryor, K. Bouchmella, L. Zhao, Y.H. Lo, M.B. Cardoso, D. Shapiro, J. Rodriguez, J. Miao, *Sci. Rep.* **2017**, *7*, 4757.
[168] R. Carzaniga, M.-C. Domart, L.M. Collinson, E. Duke, *Protoplasma* **2014**, *251*, 449.
[169] D. Drescher, T. Büchner, P. Guttmann, S. Werner, G. Schneider, J. Kneipp, *Nanoscale Adv.* **2019**, *1*, 2937.
[170] B. Kepsutlu, V. Wycisk, K. Achazi, S. Kapishnikov, A.J. Pérez-Berná, P. Guttmann, A. Cossmer, E. Pereiro, H. Ewers, M. Ballauff, G. Schneider, J.G. McNally, *ACS Nano* **2020**.
[171] S. Gil, E. Solano, F. Martínez-Trucharte, J. Martínez-Esaín, A.J. Pérez-Berná, J.J. Conesa, C. Kamma-Lorger, M. Alsina, M. Sabés, *PLOS ONE* **2020**, *15*, e0230022.
[172] P. Reineck, A.N. Abraham, A. Poddar, R. Shukla, H. Abe, T. Ohshima, B.C. Gibson, C. Dekiwadia, J.J. Conesa, E. Pereiro, A. Gelmi, G. Bryant, *Biotechnol. J.* **2021**, *16*, 2000289.
[173] M. Chiappi, J.J. Conesa, E. Pereiro, C.O.S. Sorzano, M.J. Rodríguez, K. Henzler, G. Schneider, F.J. Chichón, J.L. Carrascosa, *J. Nanobiotechnology* **2016**, *14*, 15.
[174] A. Poddar, J.J. Conesa, K. Liang, S. Dhakal, P. Reineck, G. Bryant, E. Pereiro, R. Ricco, H. Amenitsch, C. Doonan, X. Mulet, C.M. Doherty, P. Falcaro, R. Shukla, *Small* **2019**, *15*, 1902268.
[175] J.J. Conesa, J. Otón, M. Chiappi, J.M. Carazo, E. Pereiro, F.J. Chichón, J.L. Carrascosa, *Sci. Rep.* **2016**, *6*, 22354.
[176] D. Drescher, P. Guttmann, T. Büchner, S. Werner, G. Laube, A. Hornemann, B. Tarek, G. Schneider, J. Kneipp, *Nanoscale* **2013**, *5*, 9193.
[177] G.P. Szekeres, S. Werner, P. Guttmann, C. Spedalieri, D. Drescher, V. Živanović, M. Montes-Bayón, J. Bettmer, J. Kneipp, *Nanoscale* **2020**, *12*, 17450.
[178] Y. Zhu, X. Cai, J. Li, Z. Zhong, Q. Huang, C. Fan, *Nanomedicine Nanotechnol. Biol. Med.* **2014**, *10*, 515.
[179] A. Kim, W.B. Ng, W. Bernt, N.-J. Cho, *Sci. Rep.* **2019**, *9*, 2639.
[180] L. Zhang, D. Lei, J.M. Smith, M. Zhang, H. Tong, X. Zhang, Z. Lu, J. Liu, A.P. Alivisatos, G. Ren, *Nat. Commun.* **2016**, *7*, 11083.
[181] A.F. Ogata, A.M. Rakowski, B.P. Carpenter, D.A. Fishman, J.G. Merham, P.J. Hurst, J.P. Patterson, *J. Am. Chem. Soc.* **2020**, *142*, 1433.
[182] E. Yücelen, I. Lazić, E.G.T. Bosch, *Sci. Rep.* **2018**, *8*, 2676.
[183] B. Shen, X. Chen, K. Shen, H. Xiong, F. Wei, *Nat. Commun.* **2020**, *11*, 2692.
[184] Y. Zhou, X. Xu, A. Carlsson, S. Lazar, Z. Pan, Y. Ma, O. Terasaki, H. Deng, *Chem. Mater.* **2020**, *32*, 4966.
[185] S.-Y. Chen, A. Gloter, A. Zobelli, L. Wang, C.-H. Chen, C. Colliex, *Phys. Rev. B* **2009**, *79*, 104103.
[186] T. Hidalgo, M. Giménez-Marqués, E. Bellido, J. Avila, M.C. Asensio, F. Salles, M.V. Lozano, M. Guillevic, R. Simón-Vázquez, A. González-Fernández, C. Serre, M.J. Alonso, P. Horcajada, *Sci. Rep.* **2017**, *7*, 43099.
[187] S.C.B. Myneni, *Rev. Mineral. Geochem.* **2002**, *49*, 485.
[188] D.A. Shapiro, S. Babin, R.S. Celestre, W. Chao, R.P. Conley, P. Denes, B. Enders, P. Enfedaque, S. James, J.M. Joseph, H. Krishnan, S. Marchesini, K. Muriki, K. Nowrouzi, S.R. Oh, H. Padmore, T. Warwick, L. Yang, V.V. Yashchuk, Y.-S. Yu, J. Zhao, *Sci. Adv.* **2020**, *6*, eabc4904.
[189] O.L. Krivanek, N. Dellby, J.A. Hachtel, J.-C. Idrobo, M.T. Hotz, B. Plotkin-Swing, N.J. Bacon, A.L. Bleloch, G.J. Corbin, M.V. Hoffman, C.E. Meyer, T.C. Lovejoy, *Ultramicroscopy* **2019**, *203*, 60.
[190] L.K. Scheffer, C.S. Xu, M. Januszewski, Z. Lu, S. Takemura, K.J. Hayworth, G.B. Huang, K. Shinomiya, J. Maitlin-Shepard, S. Berg, J. Clements, P.M. Hubbard, W.T. Katz, L. Umayam, T. Zhao, D. Ackerman, T. Blakely, J. Bogovic, T. Dolafi, D. Kainmueller, T. Kawase, K.A. Khairy, L. Leavitt, P.H. Li, L. Lindsey, N. Neubarth, D.J. Olbris, H. Otsuna, E.T. Trautman, M. Ito, A.S. Bates, J. Goldammer, T. Wolff, R. Svirskas, P. Schlegel, E. Neace, C.J. Knecht, C.X. Alvarado, D.A. Bailey, S. Ballinger, J.A. Borycz, B.S. Canino, N. Cheatham, M. Cook, M. Dreher, O. Duclos, B. Eubanks, K. Fairbanks, S. Finley, N. Forknall, A. Francis, G.P. Hopkins, E.M. Joyce, S. Kim, N.A. Kirk, J. Kovalyak, S.A. Lauchie, A. Lohff, C. Maldonado, E.A. Manley, S. McLin, C. Mooney, M.

Ndama, O. Ogundeyi, N. Okeoma, C. Ordish, N. Padilla, C.M. Patrick, T. Paterson, E.E. Phillips, E.M. Phillips, N. Rampally, C. Ribeiro, M.K. Robertson, J.T. Rymer, S.M. Ryan, M. Sammons, A.K. Scott, A.L. Scott, A. Shinomiya, C. Smith, K. Smith, N.L. Smith, M.A. Sobeski, A. Suleiman, J. Swift, S. Takemura, I. Talebi, D. Tarnogorska, E. Tenshaw, T. Tokhi, J.J. Walsh, T. Yang, J.A. Horne, F. Li, R. Parekh, P.K. Rivlin, V. Jayaraman, M. Costa, G.S. Jefferis, K. Ito, S. Saalfeld, R. George, I.A. Meinertzhagen, G.M. Rubin, H.F. Hess, V. Jain, S.M. Plaza, *ELife* **n.d.**, *9*.

[191] D. Spehner, A.M. Steyer, L. Bertinetti, I. Orlov, L. Benoit, K. Pernet-Gallay, A. Schertel, P. Schultz, *J. Struct. Biol.* **2020**, *211*, 107528.

[192] N. Vidavsky, S. Addadi, A. Schertel, D. Ben-Ezra, M. Shpigel, L. Addadi, S. Weiner, *Proc. Natl. Acad. Sci.* **2016**, *113*, 12637.

[193] M. Elbaum, *Curr. Opin. Microbiol.* **2018**, *43*, 155.

[194] T.E. Schäffer, J.P. Cleveland, F. Ohnesorge, D.A. Walters, P.K. Hansma, *J. Appl. Phys.* **1996**, *80*, 3622.

[195] B.T. O'Callahan, K.-D. Park, I.V. Novikova, T. Jian, C.-L. Chen, E.A. Muller, P.Z. El-Khoury, M.B. Raschke, A.S. Lea, *Nano Lett.* **2020**, *20*, 4497.

[196] T. Schmid, B.-S. Yeo, G. Leong, J. Stadler, R. Zenobi, *J. Raman Spectrosc.* **2009**, *40*, 1392.

[197] N. Martín Sabanés, L.M.A. Driessen, K.F. Domke, *Anal. Chem.* **2016**, *88*, 7108.

[198] A. Nakata, T. Nomoto, T. Toyota, M. Fujinami, *Anal. Sci.* **2013**, *29*, 865.

[199] N. Kumar, W. Su, M. Veselý, B.M. Weckhuysen, A.J. Pollard, A.J. Wain, *Nanoscale* **2018**, *10*, 1815.

[200] A. Bhattarai, A.G. Joly, A. Krayev, P.Z. El-Khoury, *J. Phys. Chem. C* **2019**, *123*, 7376.

[201] A. Bhattarai, P.Z. El-Khoury, *J. Phys. Chem. Lett.* **2019**, *10*, 2817.

[202] N. Kumar, C.S. Wondergem, A.J. Wain, B.M. Weckhuysen, *J. Phys. Chem. Lett.* **2019**, *10*, 1669.

[203] C. Mayet, A. Dazzi, R. Prazeres, F. Allot, F. Glotin, J.M. Ortega, *Opt. Lett.* **2008**, *33*, 1611.

[204] M. Jin, F. Lu, M.A. Belkin, *Light Sci. Appl.* **2017**, *6*, e17096.

[205] G. Ramer, F.S. Ruggeri, A. Levin, T.P.J. Knowles, A. Centrone, *ACS Nano* **2018**, *12*, 6612.

[206] J.-M. Ortega, F. Glotin, R. Prazeres, X. Li, R. Gref, *Appl. Opt.* **2017**, *56*, 6663.

[207] G. Ramer, V.A. Aksyuk, A. Centrone, *Anal. Chem.* **2017**, *89*, 13524.

[208] M. Lewin, B. Hauer, M. Bornhöfft, L. Jung, J. Benke, A.-K.U. Michel, J. Mayer, M. Wuttig, T. Taubner, *Appl. Phys. Lett.* **2015**, *107*, 151902.

[209] A. Hermelink, D. Naumann, J. Piesker, P. Lasch, M. Laue, P. Hermann, *Analyst* **2017**, *142*, 1342.

[210] D. Partouche, J. Mathurin, A. Malabirade, S. Marco, C. Sandt, V. Arluison, A. Deniset-Besseau, S. Trépout, *J. Microsc.* **2019**, *274*, 23.

[211] L. Tetard, A. Passian, K.T. Venmar, R.M. Lynch, B.H. Voy, G. Shekhawat, V.P. Dravid, T. Thundat, *Nat. Nanotechnol.* **2008**, *3*, 501.

[212] L. Tetard, A. Passian, R.M. Lynch, B.H. Voy, G. Shekhawat, V. Dravid, T. Thundat, *Appl. Phys. Lett.* **2008**, *93*, 133113.

[213] L. Tetard, A. Passian, R.H. Farahi, T. Thundat, *Ultramicroscopy* **2010**, *110*, 586.

[214] T.F.D. Fernandes, O. Saavedra-Villanueva, E. Margeat, P.-E. Milhiet, L. Costa, *Sci. Rep.* **2020**, *10*, 7098.